Journal of Colloid and Interface Science 561 (2020) 551–567

Contents lists available at ScienceDirect

Journal of Colloid and Interface Science

journal homepage: www.elsevier.com/locate/jcis

Enhanced photocatalytic activities of polypyrrole sensitized zinc ferrite/graphitic carbon nitride n-n heterojunction towards ciprofloxacin degradation, hydrogen evolution and antibacterial studies

Kundan Kumar Das [a], Sulagna Patnaik [a], Sriram Mansingh [a], Arjun Behera [a], Ashutosh Mohanty [b], Chinmayee Acharya [c], K.M. Parida [a,*]

[a] Centre for Nano Science and Nano Technology, Institute of Technical Education and Research, Siksha 'O' Anusandhan (Deemed to be University), Bhubaneswar, Odisha 751030, India
[b] Solid State and Structural Chemistry Unit, Indian Institute of Science, Bengaluru 560012, India
[c] Environment & Sustainability Division, CSIR-Institute of Minerals and Materials Technology, Bhubaneswar 751 013, Odisha, India

GRAPHICAL ABSTRACT

Successful development of polypyrrole sensitized ZnF_2O_4/g-C_3N_4 n-n heterojunction towards Ciprofloxacin degradation, photocatalytic H_2 generation and antibacterial activity.

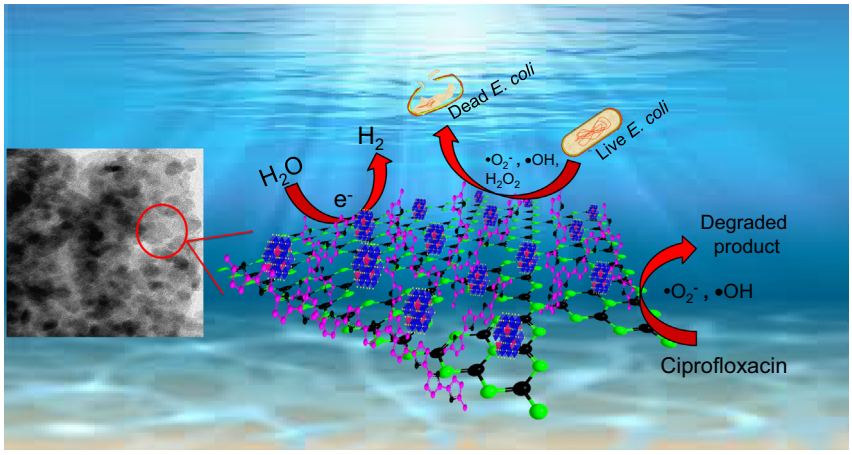

ARTICLE INFO

Article history:
Received 30 July 2019
Revised 25 October 2019
Accepted 9 November 2019
Available online 11 November 2019

Keywords:
ZFCN@20PPY
Polypyrrole
Ciprofloxacin degradation

ABSTRACT

Fusion of heterogeneous photocatalysts with conducting polymers has paid a rising stratagem in the field of photocatalysis owing to its biocompatibility and environment friendliness. In this work a series of polypyrrole (PPY) sensitized zinc ferrite/graphitic carbon nitride (ZFCN) n-n heterojunction (ZFCN@10PPY, ZFCN@20PPY, and ZFCN@30PPY) nanocomposite were fabricated by in-situ polymerization method. Due to low band gap of polypyrrole, it behaves as a photo-sensitizer, supplies surplus numbers of electrons to $ZnFe_2O_4$/g-C_3N_4 n-n heterojunction and improves the photocatalytic performance. The fabricated ZFCN@20PPY exhibits highest photocatalytic activity in comparison to others nanocomposites. The superior photocatalytic performance of ZFCN@20PPY was ascribed to the tunable band structure, synergistic effect of broad absorption upto NIR region, delayed electron-hole recombination and

* Corresponding author.
E-mail address: kulamaniparida@soauniversity.ac.in (K.M. Parida).

https://doi.org/10.1016/j.jcis.2019.11.030

Hydrogen evolution
Antibacterial activity achievement

efficient charge transfer across the junction interface which has been well confirmed from UV–Vis DRS, PL and EIS measurement. Further the photocatalytic activity of ZFCN@20PPY was supported by both n-type and p-type photocurrent density i.e. 2.4 and 3.9 mA/cm^2 respectively. ZFCN@20PPY shows good photocatalytic performance towards ciprofloxacin degradation (92%) and generation of hydrogen energy (567 μmol). Along with pollutant degradation and energy production ZFCN@20PPY also shows its potential towards antibacterial activities against human pathogenic bacteria like *Escherichia coli*. These newly designed polymer sensitized n-n heterojunction may offer a promising strategy for maximum light absorption and be authoritative in meeting the environmental claims in the future.

1. Introduction

In the present scenario, industrialization and population growth are the two factors that have forced the world to suffer from various problems like high energy demand, depleting power resources and environmental issues. Coal, oil and natural gas are the leading fossil fuels that are readily available to solve the hunger of energy requirement [1–4]. However, these fossil fuel energy resources wholly don't meet the requirement of a vast growing society rather its extensive consumption leads to the depletion of resources. Additionally, the burning of fuels produces harmful gases which are accountable for ecological devastation with harmful environmental impacts [3]. Apart from the energy crisis, now-days, water pollution has also become a major point of concern. Ciprofloxacin (CIP) is one of the antibiotic products used to treat bacterial infections. Extensive utilization and discharge of CIP from pharmaceutical industries and hospitals without any treatment affects the aquatic ecosystem and results in environmental pollution [5–7]. Therefore, finding a greener and sustainable way to resolve these problematic outcomes is a big question mark for the scientific society. Semiconductor based photocatalyst is an answer to the asked question, as it uses plentiful of eco-friendly solar energy to produce H_2 gas from water splitting reaction and also mineralize the pollutant into CO_2 and H_2O [8–16].

In recent years, various spinel structure ferrite photocatalysts have been extensively used for H_2 production and degradation of organic pollutants. Enclosing the advantages of spinel like a visible light response, internal magnetic properties, stupendous stability and availability of numerous photo-active sites, $ZnFe_2O_4$ nanoparticles (with the narrow band gap of 1.9 eV) among all ferrites have the potential to behave as a proficient photocatalyst [17,18]. Still, the photo-catalytic potential of $ZnFe_2O_4$ is not up to the dreamed target due to the fast recombination of photogenerated excitons in the spinel crystal structure. As a result, $ZnFe_2O_4$ cannot be used as a single photocatalyst and wishes for some modifications. The modification of $ZnFe_2O_4$ by forming composites with other metal oxides, noble metals, doping with different metals and non-metals, constructing heterojunction photocatalysts, etc has resolved the problem to a marginal extent [17,19]. Still, among all these modifications, constructing a heterojunction photocatalysts have been broadly valued, as it provided an effective way to improve the photocatalytic activity by constructing a built-in electric field at the interface to diminish the charge recombination process. To serve the purpose, graphitic carbon nitride (g-C_3N_4) a metal-free photocatalyst has attracted attention in the fabrication of heterojunctions in the entire scientific society because of its distinctive features like chemical &thermal stability, faster charge transport, and optical properties to absorb light in visible range [20–23]. But, very recently some research groups including our present investigation ($ZnFe_2O_4$/g-C_3N_4 heterojunction) have observed that the photocatalytic activities of heterojunction based systems were not up to the bench-mark and deserve further modification to augment the photocatalytic performance [24–26]. Therefore, modification of heterojunction materials with a conducting polymer-like, polypyrrole, polyaniline, etc is emerging as a new strategy. In this view, Polypyrrole (PPY) is a classical organic conducting polymer which belongs to a nitrogen-rich family exhibiting interesting redox properties, extraordinary stability, and an environmentally friendly and easy way to synthesis. Polypyrrole also exhibits high electrical conductivity due to the presence of a large number of π- conjugated backbones which facilitates better charge transformation in a photocatalytic process [20]. Lastly, such a newly photocatalyst (i.e. PPY sensitized $ZnFe_2O_4$/g-C_3N_4 n-n heterojunction) yet had not been reported to date for photocatalytic and bacterial application.

In the current study, polypyrrole sensitized $ZnFe_2O_4$/g-C_3N_4 n-n heterojunction has been designed by the in-situ polymerization method. The in-situ approach of a polymer-modified n-n heterojunction facilitated in improving conductivity and charges separation via lower band gap sensitizing behavior of polypyrrole. Impressively, compared with simple heterojunctions, the polypyrrole sensitized $ZnFe_2O_4$/g-C_3N_4 n-n heterojunction provided dramatically improved photoelectrochemical studies like LSV and EIS. Furthermore, PPY sensitized $ZnFe_2O_4$/g-C_3N_4heterojunction photocatalyst showed excellent results in water reduction reaction for hydrogen generation, degradation of CIP and antibacterial activities against human pathogenic bacteria like *Escherichia coli* (ATCC 8739) under visible light irradiation.

2. Results and discussion

2.1. Crystal structure

Fig. 1 displays the characteristic XRD pattern of as-synthesized PPY, CN, ZF, ZFCN, and nanocomposites ZFCN@XPPY(X = 10, 20 and 30 wt%). In detail, neat polypyrrole exhibit a broad peak at 2θ = 25.68°, which suggests its amorphous like character (Fig. 1a) [27]. Further, in Fig. 1b two strong and prominent diffracted peaks were observed for g-C_3N_4 at Braggs angle 27.5°(0 0 2) and 12.95°(1 0 0), where the former is attributed to melon type of networks present in the conjugated aromatic system and the later arises due to structural packing of in-planar tri-s-triazine units respectively [18]. The obtained diffraction peaks of pure $ZnFe_2O_4$ are seen at 2θvalues 29.9°, 35.21°, 42.79°, 53.14°, 56.66°and 62.13° which can be assigned to scattering from (2 2 0), (3 1 1), (4 0 0), (4 2 2), (5 1 1) and (4 4 0) planes respectively [28]. Additionally, the observed XRD pattern of $ZnFe_2O_4$ implies formation of single cubic phase with spinel structure as per JCPDF no. (01-077-0011). In comparison to pure zinc ferrite, the characteristic XRD peaks of ZF in ZFCN composite (1:2) displays a significant reduction in diffraction peak intensities and also a slight shift in peak position to higher angle suggests that CN contents play a dominance role over crystalline phases of cubic spinel. Similarly, the intensity of (1 0 0) plane of pure CN has been decreased in the case of ZFCN. This visualized shifting and reduction of diffrac-

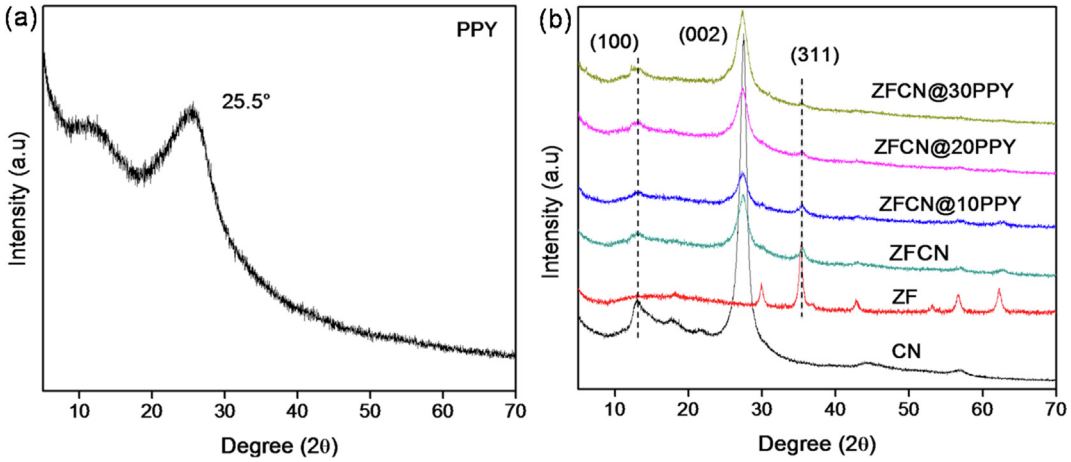

Fig. 1. XRD patterns of (a) PPY (b) CN, ZF, ZFCN, ZFCN@10PPY, ZFCN@20PPY and ZFCN@30PPY.

tion peaks of zinc ferrite and C_3N_4confirms the successful formation of ZFCN heterojunction. Furthermore, upon polymerization the intensity of (3 1 1) plane of ZF decreases in ZFCN@PPY with increasing the polypyrrole percentage as compared to ZF and ZFCN as shown in Fig. 1b. But, the signature peak of pure polypyrrole was not seen in the ternary composite (ZFCN@PPY) which indicates about well dispersion and distribution of polymer within the binary system. Interestingly, no other peaks except (3 1 1) facet of ZF are visible in 10, 20 and 30% of ZFCN@PPY composites which suggest that polymerization process and increasing amount of pyrrole hinders the crystal growth of spinel ZF. However, the intensity of CN peaks has been found to increase with increasing the polymer amount in ZFCN@PPY composites.

2.2. Light harvestation property

The optical properties which greatly influence the catalytic activity of the designed materials (CN, ZF, ZFCN, PPY, and ZFCN@PPY samples) were measured by UV–Vis diffuse reflectance spectrophotometer and the obtained results are represented in Fig. 2. Fig. 2a shows that pristine g-C_3N_4 exhibits narrow spectra in the blue region of the visible spectrum with an absorption edge at 464 nm arising for two reasons (i) electronic charge transmission from N_{2p} orbitals to C_{2p} orbitals and (ii) due to n–π^*transitions within triazine rings [20,29]. It can be seen that, pure ZF displays a wide range of absorption spectra ranging between 200 and 700 nm due to photo-excitation of electrons from O_{2p} to Fe_{3d} state [28]. However, ZFCN composite displays a wide range of solar spectrum absorbance extends upto 600 nm and exhibits a significant bathochromic shift in comparison to pure CN which was attributed to the colored properties of ZF. These results inform about the coexistence of ZF and CN within the formed binary composite. Similarly Fig. 2b shows that polypyrrole exhibits a strong absorption band around 600–620 nm which is due to the existence of —NH— species, and presence of bipolaron band transitions [30]. Similar fashion was observed for all the ternary composites (ZFCN@PPY) after the introduction of various weight percentage of polypyrrole into ZFCN, that improves the light harvesting ability and hence all composites tends to cover entire solar spectrum starting from the ultraviolet region to near infrared region. The optical band gap energies of all the photocatalyst are calculated via the Kubelka-Munk equation and the obtained data were given in Fig. S1.

2.3. Morphological study

2.3.1. TEM & HR-TEM

TEM and HR-TEM measurements were conducted to explain the internal morphology, crystal phase, planar spacing and microscopic structure of the synthesized pristine nanomaterials and its respective composites. Fig. S2a reveals that the particles of pristine ZF are observed to be non-uniform in size (around 30–40 nm), in agglomerated form and displays quasi-spherical type morphology.

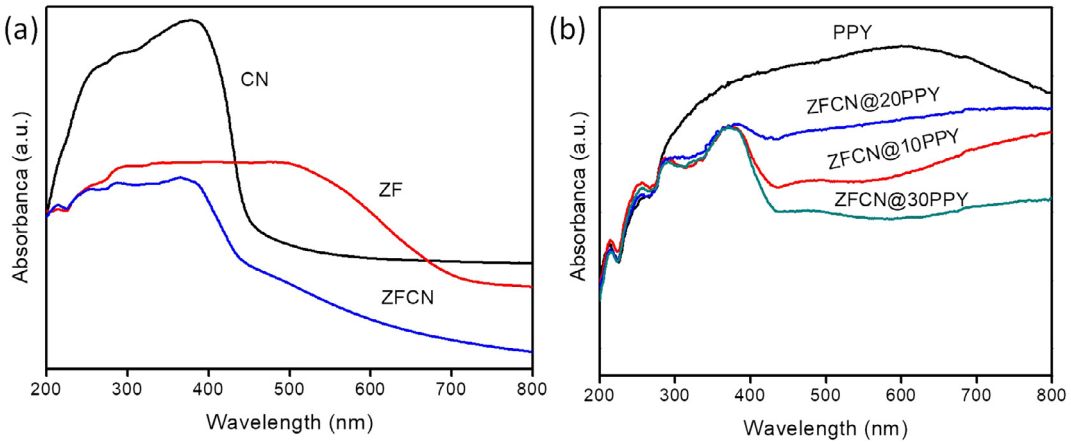

Fig. 2. UV–vis spectra of as-synthesized (a) CN, ZF and ZFCN (b) PPY, ZFCN@10PPY, ZFCN@20PPY, and ZFCN@30PPY.

HR-TEM image shown in Fig. S2b depicts two inter-layer spacing d value of 0.29 and 0.25 nm, which matches well with (2 2 0) and (3 1 1) facets of cubic ZF respectively [17]. The well-developed crystallinity of ZF is further confirmed from the observed concentric circles representing (2 2 0) and (3 1 1) crystal planes in selected area electronic diffraction (SAED) pattern (Fig. S2c). As shown in Fig. S2d, pure CN displays stacks of porous sheet like structure and the stacking of these CN sheets is due to strong *Van der Waals* force of interaction which exists between the aromatic system and tri-s-triazine units. Further, the SAED pattern of CN displays the circular ring that can be ascribed to (0 0 2) plane explaining its polycrystalline characteristics shown in Fig. S2e [31]. Micrograph picture of pure polypyrrole has been demonstrated in Fig. S2f which exhibit typical sphere-like structure in an agglomerated form. In low magnification a cloud-like appearance of PPY was observed which may be due to the co-existence of strong Van der Waals force of attraction. No sign of crystallinity was obtained from HR-TEM and SAED images (Fig. S2g) which strongly confirms the amorphous nature of the material. Additionally, the TEM images of ZFCN@20PPY were illustrated in Fig. 3, which highlights good interaction between ZF, CN and PPY. It is seen that in ZFCN@20PPY, similar cloud-like visualization was observed for polypyrrole (Fig. 3a). The distribution of polypyrrole particles in the composite has been well demarcated. The sheet-like morphology was retained by carbon nitride even after the formation of composite. The presence of dense black color particles in the image confirms the existent of ZF within the composite. The image reveals that attachment of both ZF and PPY onto the surface of CN may be due to strong electrostatic attraction and chemical bonding with CN through hydrogen atoms. Moreover, the HRTEM picture of ZFCN@20PPY shows clear and distinct lattice fringes with d-spacing value of 0.25 nm and 0.29 nm which can be indexed as (3 1 1) and (2 2 0) crystal facets of cubic ZF and d-spacing value of 0.32 nm representing (0 0 2) facet of CN confirms that both ZF and CN retains their crystalline nature in the ternary hybrid. The HRTEM image also shows the interconnect lattice fringes of ZF and CN which confirms the formation of heterojunction structure rather than a simple attachment. In addition, the availability of (0 0 2), (2 2 0) and (3 1 1) planes from SAED pattern confirms the polycrystalline nature and presence of both ZF and CN in ZFCN@20PPY. Very few lattice fringes are available for ZF in the composite which indicates that loading of polymer hampers the crystalline nature of the material which is well matched with our XRD data. Moreover, the TEM measurement indicates the existence of good interconnection between ZF, CN, and PPY which helps in effective charge separation and transfer in ZFCN@20PPY hybrid. This process of exciton separation and movement plays a key role in enhancing the photocatalytic activity.

2.3.2. SEM

Fig. (S3a, b) depicts both low and high magnification SEM images of pristine ZF. Solid block-like appearance with irregular shape and size was observed from the low magnification view. From high magnification, it can be seen that the surface of ferrite material contains a good number of fine pores or void spaces indicating the porous nature of the material. The formation of fine pores within the material is may be due to the discharge of huge amount of gases (CO_2, CO, and H_2O) and the elimination of organic matter at the time of calcination. Further, during thermal combustion, some gases may be present within the material which have not escaped and results in the formation of deep well like structure and inhibits the formation of pores/voids in some portions [32]. The SEM images of neat CN (Fig. S3c) illustrates a layered and sheet-like structure with pores, is in good agreement with TEM results. Moreover, the sheets are found to be thin and in an irregular shape. The SEM images of pristine PPY (Fig. S3d) exhibits a group of spherical structures in an agglomerated form with large sized particles. This may be due to the addition of APS as an oxidizer which is responsible for the growth of such type of compact microstructure [33]. Higher and lower magnification SEM images

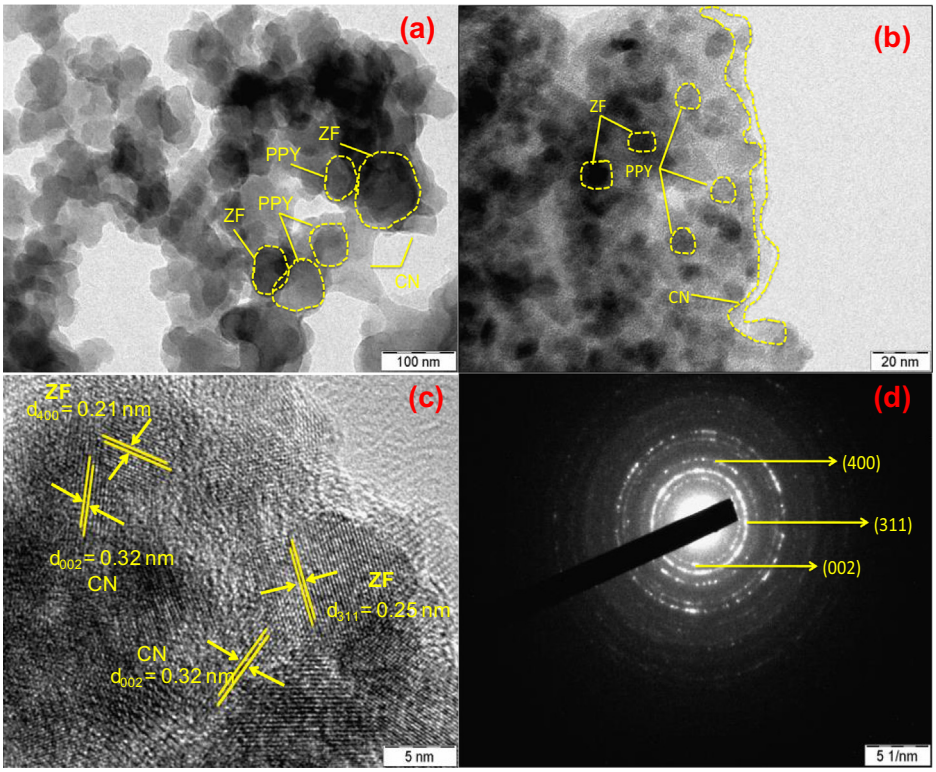

Fig. 3. Representative micrographs of ZFCN@20PPY (a and b) TEM, (c) HRTEM, (d) SAED pattern.

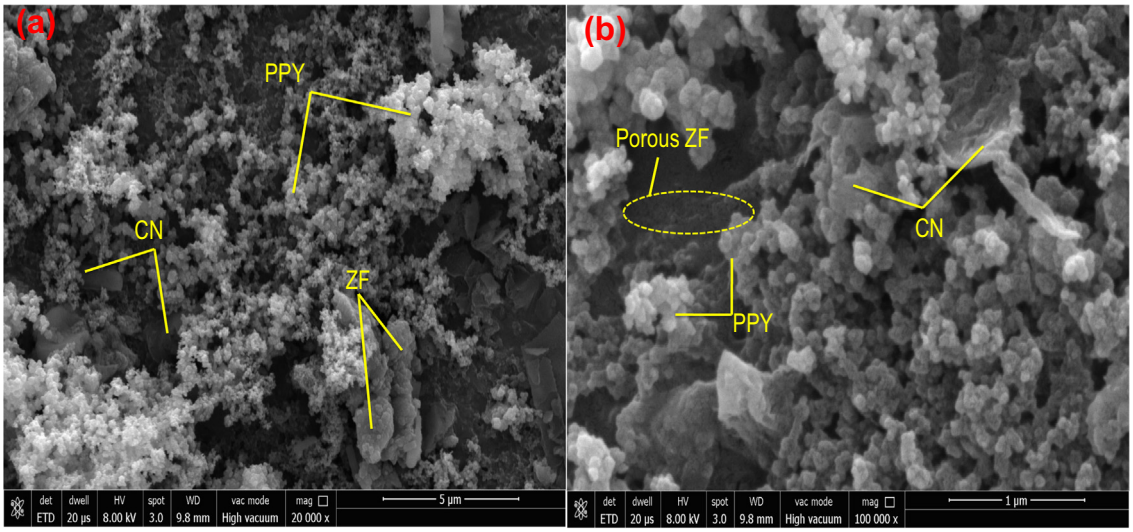

Fig. 4. Low and High magnification SEM micrographs of ZFCN@20PPY (a and b).

of ZFCN@20PPY in Fig. 4, explains the topology of the material. Thin sheets with a smooth surface of CN can be seen from the lower magnification image (Fig. 4a). Strong anchoring of ZF particles on the surface of CN sheets was observed from the image. An agglomerated network of polypyrrole was also observed, which were well attached and distributed over the ZFCN. On high magnification, pores on ZF and CN sheet were noticed and been well-demarcated (Fig. 4b).

2.4. FTIR analysis

To explore the types of molecular vibrational modes (stretching and bending) and to validate the existence of various functional groups within the synthesized nanomaterials, IR characterization was carried out. Fig. 5 displays the IR spectra of all the prepared photocatalysts within the range of 4000–400 cm^{-1}. Pure ZF exhibits two IR characteristic bands at 435 and 554 cm^{-1} which represents the stretching and breathing modes of Fe—O and Zn—O groups at octahedral and tetrahedral sites [28,34]. The trademark band of pure polypyrrole is located at 1552 and 1467 cm^{-1} corresponds to the C=C and C—C stretching band of benzenoid and quinoid framework present in the pyrrole ring [35]. The IR band positioning at 1130 cm^{-1} represents the bending mode of the pyrrole ring while 1046 cm^{-1} symbolizes the C—H deformation. Moreover, the bands located at 787 and 932 cm^{-1} validates the presence of polymerized pyrrole [36]. Similarly, pristine CN represents all IR blueprints of aromatic carbon and nitrogen heterocycles which informs about the formation of graphite-like-sp2 structural units. CN exhibits a broad range of transmittance between the region of 3100–3500 cm^{-1} confirming the existence of primary and secondary amine groups along with surface absorbed water hydroxyl groups [37]. Additionally, CN shows small characteristic peaks in the range of 1200–1600 cm^{-1}, which were mainly attributed to the stretching vibrations of C—N aromatic rings [10]. Adding more it, a highly intense absorption band is encountered at approximately 805 cm^{-1} that symbolizes the breathing modes of triazine and heptazine rings, which represents the co-existence of a melon entity with —NH/—NH_2 groups [37]. In ZFCN similar type of stretching and breathing modes was also observed, suggesting the presence of both materials in the composite. In ZFCN, the breathing mode of triazine units at 805 cm^{-1} shifts to higher wave-number which signifies the existence of chemical bonding and close electronic interaction between ZF and CN rather than simple physical attachment [38]. All the characteristic bands of CN, ZF, and PPY are retained in the ZFCN@20PPY composite, further confirms the presence of all key constituents within the composite nanomaterial. The characteristic band of polypyrrole shifts to 1477 cm^{-1} in the ternary composite i.e. ZFCN@20PPY and this shifting of the band indicates the formation of hydrogen bonding and π-π interaction between surface CN and PPY ring structure [39]. Similarly, the intensity of the triazine unit is reduced in ZFCN@20PPY composite as compared to CN and ZFCN. The band shifting and reduction of peak intensities desperately informs about good interaction and electron movement between the composite ZFCN heterojunction and the polymer itself.

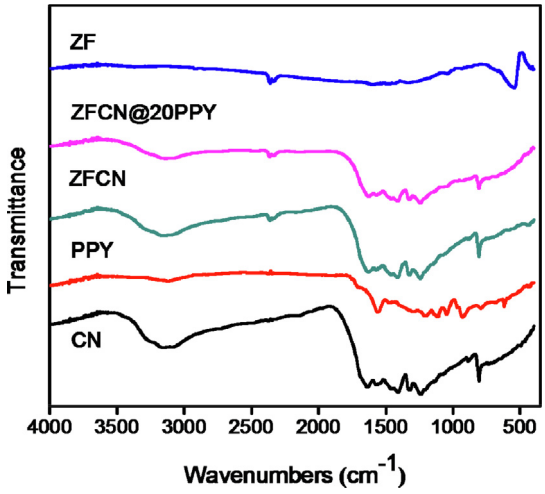

Fig. 5. FT-IR transmittance spectra of PPY, CN, ZF, ZFCN, ZFCN@10PPY, ZFCN@20PPY and ZFCN@30PPY.

2.5. XPS & EDX

In order to explore more details about composition, electronic environment, valence states of the elements and bond interaction of as-synthesized ternary ZFCN@20PPY nanocomposite, XPS characterization was carried out. Further the deconvoluted (via Cassa XPS software) XPS spectra of C 1s, O 1s, Fe 2p, Zn 2p and N 1s of the analyzed sample were portrayed in Fig. 6. The photoelectron peaks of C, O, Fe, Zn and N elements were identified from the sur-

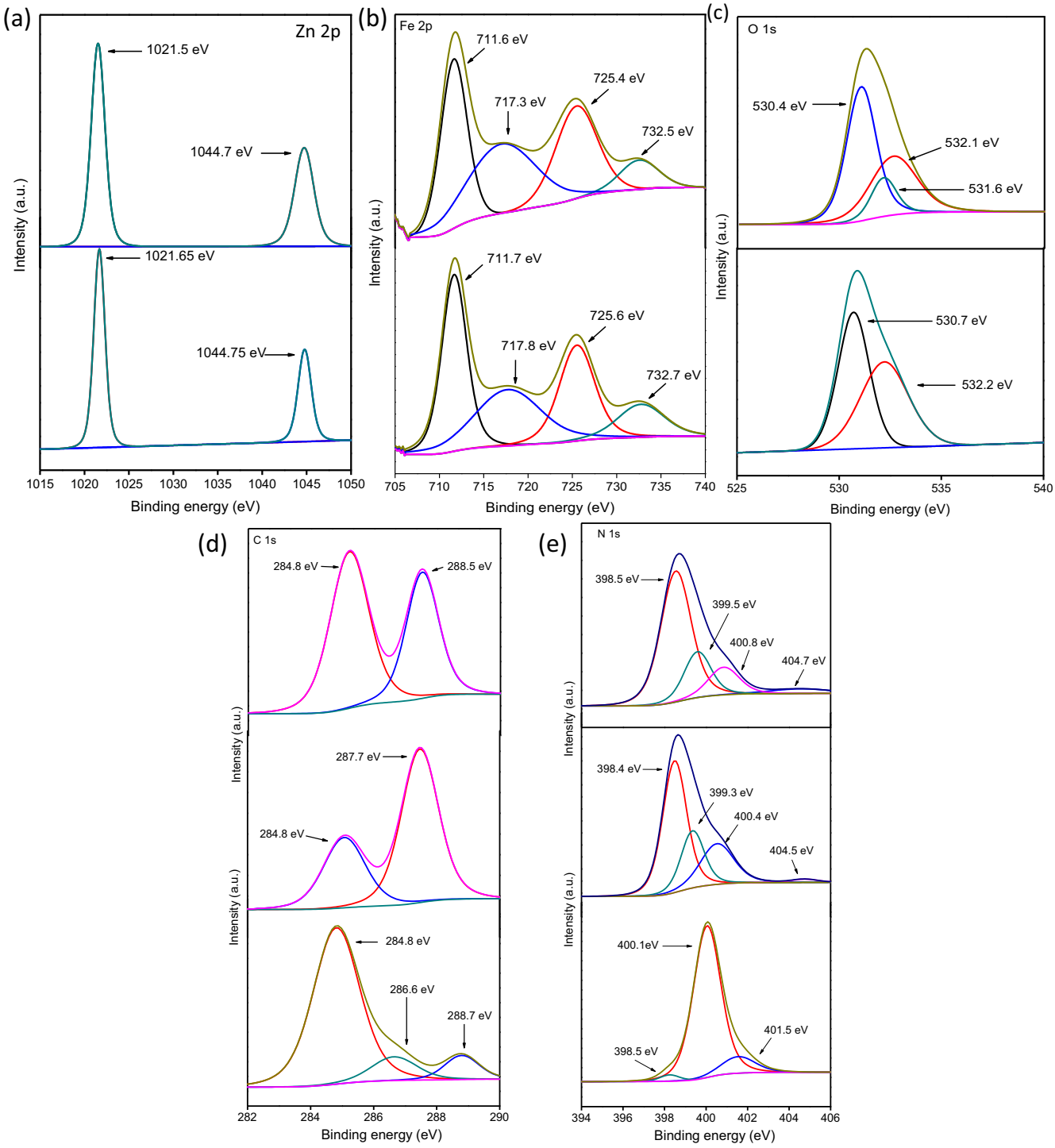

Fig. 6. High resolution XPS spectra of (a) Zn 2p, (b) Fe 2p, (c) O 1s, (d) C 1s and (e) N 1s.

vey spectrum provided in S4 confirming the elemental content. In pristine $ZnFe_2O_4$, Zn exhibits two prominent peaks at binding energies 1021.65 and 1044.75 eV corresponds to Zn $2p_{3/2}$ and Zn $2p_{1/2}$ spin states respectively and confirming the existence of Zn in 2^+ state [40]. Furthermore, peak-fitted Zn 2p spectrum of ZFCN@20PPY was examined to know the nature of the Zn phase as well as its interaction with CN and PPY. After the formation of composite, the corresponding Zn 2p peaks of ZFCN@20PPY were found to be shifted towards a lower BE of 1021.5 and 1044.7 eV shown in Fig. 6a. Similarly Fe in neat $ZnFe_2O_4$ displays two distinct peaks at 711.7 and 725.6 eV which symbolizes the presence of Fe^{3+} species [40]. However for ZFCN@20PPY, the Fe 2p peak shows a red shift and displayed two characteristic peaks at 711.6 and 725.4 eV related to Fe $2p_{3/2}$ and Fe $2p_{1/2}$, respectively (Fig. 6b). This indicates that both Zn and Fe are present in form of Zn^{2+} and Fe^{3+} chemical states in composite ZFCN@20PPY. The O 1s spectrum of pristine ZF is compared with that of composite ZFCN@20PPY shown in Fig. 6c. The O 1s spectrum in pure ZF could be deconvoluted into two peaks situated at 530.7 eV and 532.2 eV. The peak centered at 530.7 eV can be related to lattice oxygen and reflects the Fe—O

and Zn—O bonds specifically [41,42]. The other peak found at 532.2 eV can be ascribed to the absorbed oxygen species like O^- and O_2^- respectively [43]. While the O 1s spectra of ZFCN@20PPY reveals three peaks ascribed to the lattice oxygen of metal center (530.4 eV), formation of hydroxyl groups (531.6 eV) and absorbed water (532.1 eV). However, a negative shift of O 1s spectra in the composite can be visualized which confirms about good interaction between the elements present in the ternary system. Moreover, the presence of O—H group indicates the formation of ZFCN heterojunction within the ZFCN@20PPY composite [44]. Fig. 6d demonstrates the deconvoluted carbon C1s spectrum of pure PPY, CN, and composite ZFCN@20PPY. The pure polymer exhibit three main signals positioned at 284.8, 286.6 and 288.7 eV while neat CN displays two peaks with binding energies values of 284.8 and 287.7 eV. However, two C 1s peak could be observed for ZFCN@20PPY with slight shifting. The peak at 284.8 eV can be ascribed to the sp2 hybridization of impure carbon concentration while the second peak (288.5 eV) is due to the sp^2 hybridized carbon with N—C=N coordination respectively [45–47]. Similarly Fig. 6e demonstrates the XPS spectra of N 1s for both the blank and composite. Going insight, the solid peaks traced at 398.5, 400.1 and 401.5 eV for polymer can be ascribed to immine structure, neutral nitrogen present in pyrrole ring and positively charged polaron species [45]. The N 1s spectra of CN reveals four deconvulated peaks located at 398.4, 399.3, 400.4 and 404.5 eV. But in the case of composite ZFCN@20PPY, N1s spectra can be fitted into four peaks at 398.5, 399.5, 400.8 and 404.7 eV as shown in Fig. 6d. The principal peak at 398.5 eV symbolizes sp2-hybridized atoms (C=N—C) as well as stands for quinoid amines (=N—) [10,18]. While the peak at 399.5 eV can be ascribed to N—$(C)_3$ groups linked with heptazine ring (C_6N_7) along with benzenoid amine (—NH—) groups [18,34]. The peak at 400.8 eV is due to the N of N—$(C)_3$ in aromatic cycles and protonated benzenoid amine groups of PPY [48]. And a small hump is seen at 404.7 eV which is because of π excitations [34]. In comparison to N1s of pure CN and PPY, a positive shift can be observed in composite, which suggests the constituent of the ternary hybrid is linked well with each other. From the above discussions, it was observed that Zn, Fe and O in composite exhibits a red shift in the positions of BE while a blue shift was observed in the binding position of CN and PPY. The blue shifting of binding energies is may be due to the transfer of electrons from PPY and CN to ZF. These spectacles have enhanced the electron mass of ZF in the nanocomposite and cause a lower BEs of Zn, Fe, and O respectively. Likewise, the decreased electron concentration of PPY and CN in composite ZFCN@20PPY causes an increment in BE of N and C elements. Additionally, the occurrence of Zn, Fe, O, N and C were confirmed from EDX analysis (Fig. S5), and well-matched with the XPS survey scan.

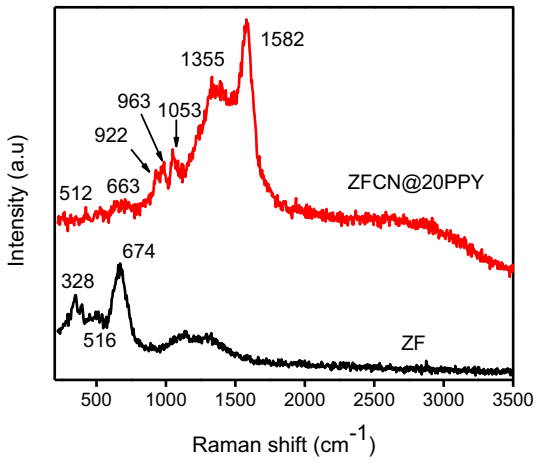

Fig. 7. Raman Spectra of ZF and ZFCN@20PPY.

2.6. Raman study

Raman spectroscopy is believed to be a strong and powerful characterizing tool to the evaluate structure, interaction, defect and electronic status of the materials. A polarization study is carried out to determine the formation of nanocomposite along with to determine the type of interaction and defects present within the synthesized sample. Fig. 7 illustrates the Raman findings of ZF & ZFCN@20PPY photocatalyst. ZF corresponds to spinel ferrite family with Fd3m space groups [17]. As observed from the plotted Raman data, all three vibrational modes located at 340, 488 and 636 cm^{-1} represents the symmetric vibrational states of cubic spinel structure. Moreover, the highlighted Raman mode above and below 600 cm^{-1} suggests the existence of tetrahedral AO_4 and octahedral BO_6 groups respectively [17]. Similarly pristine PPY exhibits two broad and distinct Raman peaks positioning at 1345 and 1561 cm^{-1} as given in S6a. The peak encountered at 1561 cm^{-1} was attributed to C=C backbone stretching arising from sp^2 hybridized carbon groups present in the polypyrrole. The obtained peak is quite similar to the "G band" of graphene. Another band is located around 1350 cm^{-1} that corresponds to the antisymmetrical C—N stretching [49]. Apart from two strong peaks, no other peaks were found in pure polypyrrole. Moreover, no Raman peaks were obtained for pure CN as shown in S6b, which confirms it to be a Raman inactive material. The ZFCN@20PPY also demonstrates similar types of Raman signals as observed in the case of pure polypyrrole with the existence of ZF polarization bands, which evidenced the successful formation of the composite. However, a weeny shift alongside reduced intensities was observed for ZF and PPY Raman bands which confirms the good interaction within the composite. Along with the characteristic peak, some additional peaks also observed in ZFCN@20PPY positioned at 922, 963 and 1053 cm^{-1} which are due to the bipolarons and polarons vibrational ring structure of PPY along with symmetrical C—H in-plane deformation modes of aromatic rings [48].

2.7. N_2 Isotherm

The porous character of graphitic carbon nitride and ZF is somehow revealed from TEM and SEM measurements/characterization but the details textural properties of the synthesized photocatalysts were measured by the BET method using nitrogen adsorption-desorption isotherms carried out at 77 K. The obtained data of specific surface area (S_{BET}), pore size distribution (PSD) and pore volume are précised and given in Table 1. The nitrogen physiosorption isotherms of samples are given in Fig. 8. Further, Fig. 8a displays that all synthesized samples reveal the type IV adsorption branch according to BDDT taxonomy, indicating the presence of a porous network which may be due to capillary condensation [50]. All samples show an H3 type loop which indicates the development of slit-shaped pores originating from the aggregated particles along with narrow pore size distribution between 2 and 10 nm

Table 1
Textural property of ZF, PPY, CN, ZFCN, ZFCN@20PPY.

Samples	Surface area [$m^2 g^{-1}$]	Pore volume [$cm^3 g^{-1}$]	Mean Pore diameter [nm]
ZF	43.64	0.12	6.96
CN	20.34	0.04	9.1
PPY	21	0.02	1.86
ZFCN	23.6	0.04	4.02
ZFCN@PPY	29.52	0.05	1.86

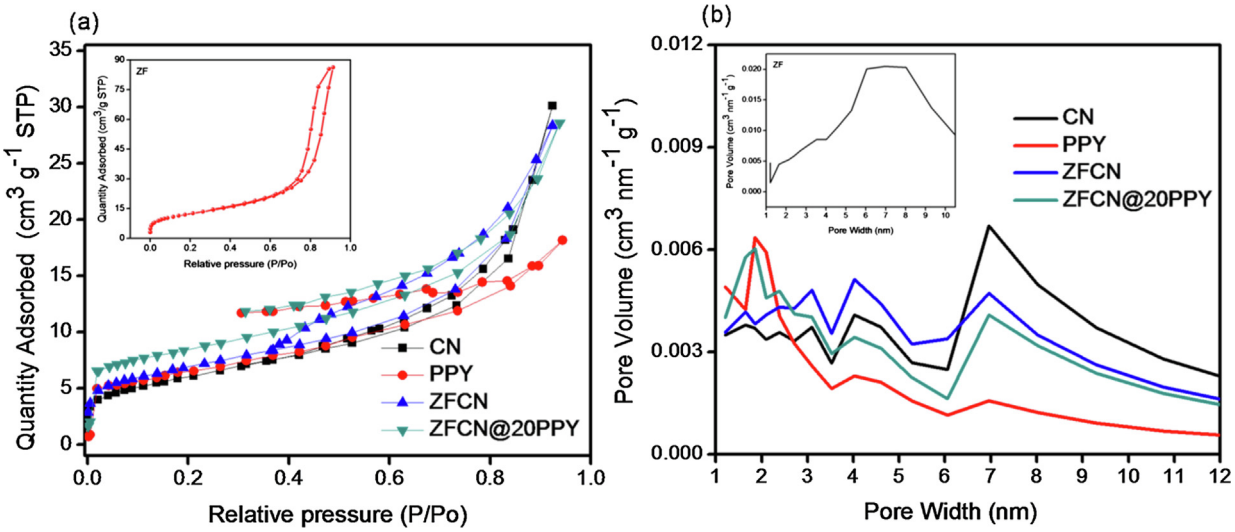

Fig. 8. (a) N_2 adsorption-desorption isotherm of ZF (inset), PPY, CN, ZFCN, ZFCN@20PPY (b) pore size distribution of ZF (inset), PPY, CN, ZFCN, ZFCN@20PPY.

as measured from BJH curves as depicted in Fig. 8b. The total pore volume for all the samples was calculated at $P/P_0 = 0.93$. The ZFCN@20PPY shows more surface area as compared to pristine CN, PPY, and ZFCN but less than pure ZF. The high specific area of ZF may be due to the thermal decomposition of zinc and iron oxalate at a high temperature which results in the release of gaseous products and the outcomes of these reactions leads to the formation of a porous structure along with enhanced surface area. In the case of ZFCN, the surface area decreases in comparison to pure ZF which can be attributed to the blocking some part of pores by an excessive amount of CN. But in ZFCN@20PPY, the BET area increases slowly to 26 $m^2\ g^{-1}$ as compared to ZFCN. The enhancement of surface area is may be due to the addition polypyrrole structure over ZFCN during the polymerization reaction.

2.8. Photocatalytic activity

2.8.1. Photocatalytic activity towards degradation of ciprofloxacin under solar light irradiation

Finally, the photocatalytic efficiency of the synthesized nanomaterials was checked towards the degradation of antibiotic ciprofloxacin (CIP) under visible light exposure and the comparative outcomes are demonstrated in Fig. 9. CIP degradation was also carried out in the absence of a catalyst to check its self-degrading properties and the desired outcome suggests that the self-photolysis of CIP can be neglected. The highest rate of CIP degradation is encountered for ZFCN@20 PPY, which is about 92% in comparison to other synthesized photocatalysts under the same reaction condition. ZFCN@20PPY displays the highest photocatalytic activity which can be attributed to the decorated polypyrrole which acts as sensitizer and harvests more light and also to the formed ZFCN heterojunction that effectively separates and channelizes the photo-generated excitons and made them available in respective places to carry out the performed photocatalytic reaction (Fig. 9a). Fig. 9b depicts the consequence of visible light illumination time upon CIP concentration and it was found that with increasing the irradiation time the concentration of CIP gradually decreases. The maximum degradation (lowest concentration of pollutant) was obtained for 120 min of visible light illumination. To determine the kinetics, the rates of CIP degradation were screened at a regular time interval. Fig. 9c illustrates the photocatalytic degradation of CIP, that follows pseudo- first order kinetics and the respective kinetic equation is as follows:

$$-\ln(C/C_0) = \text{kappt}.$$

where C represents the concentration after time t, C_0 is the initial concentration and Kaapt is the apparent rate constant of the reaction process. A negative slope is obtained by extra-plotting ln (C_0/C) with respect to time which provides information about the apparent rate constant K and the apparent constant K values of the photocatalysts were calculated from the obtained slope and the values are represented in Table 2. The result shows that among all photocatalysts ZFCN@PPY20 is more efficient in degrading the pollutant. The reason behind this scenario can be ascribed to strong absorption of visible light, availability of more number of active sites and proper channelization of photo-generated charge carriers and good interaction between the materials. The absorption spectra of ZFCN@20PPY at different time intervals were determined by UV–Vis spectrophotometer and the obtained outcomes were portrayed in Fig S7a. From figure it was clear that with an increase in reaction time, the absorption peak gradually decreases which confirms the degradation of ciprofloxacin. Further, the degradation of CIP was again confirmed from HPLC analysis as provided in Fig. S7b. Moreover, the CIP mineralization was estimated over ZFCN@20PPY at a consistent interval of time by performing TOC measurement. The mineralization magnitude with respect to time was represented in Fig. S7c. From the TOC plot, it was observed that ZFCN@20PPY can effectively remove TOC 78% within 120 min of reaction.

2.8.1.1. Effect of ciprofloxacin concentration. The initial concentration of the pollutant has been found to affect the photodegradation activity. The effect of the initial concentration of the pollutant has been evaluated by using ZFCN@PPY20 photocatalyst and the outcomes were depicted in Fig. 9d. From figure it can be noticed that degradation efficiencyof ZFCN@20PPY decreases with an increase in the pollutant concentration. The decrease in the degradation rate of the pollutant can be ascribed to various reasons. First of all, with increasing the ciprofloxacin concentration, the availability of ciprofloxacin molecules will be more in comparison to the active sites present on the surface of the catalyst. Infiltration of visible light may also hampers the degradation efficiency of the catalyst as higher pollutant concentration will create a certain type of barrier between the catalyst and light source. This will reduce the infiltration of visible light into the reaction system and led to low adsorption of the photon on the catalyst surface for reaction to occur. Moreover, a high concentration of pollutants will produce a huge amount of intermediates that may further compete

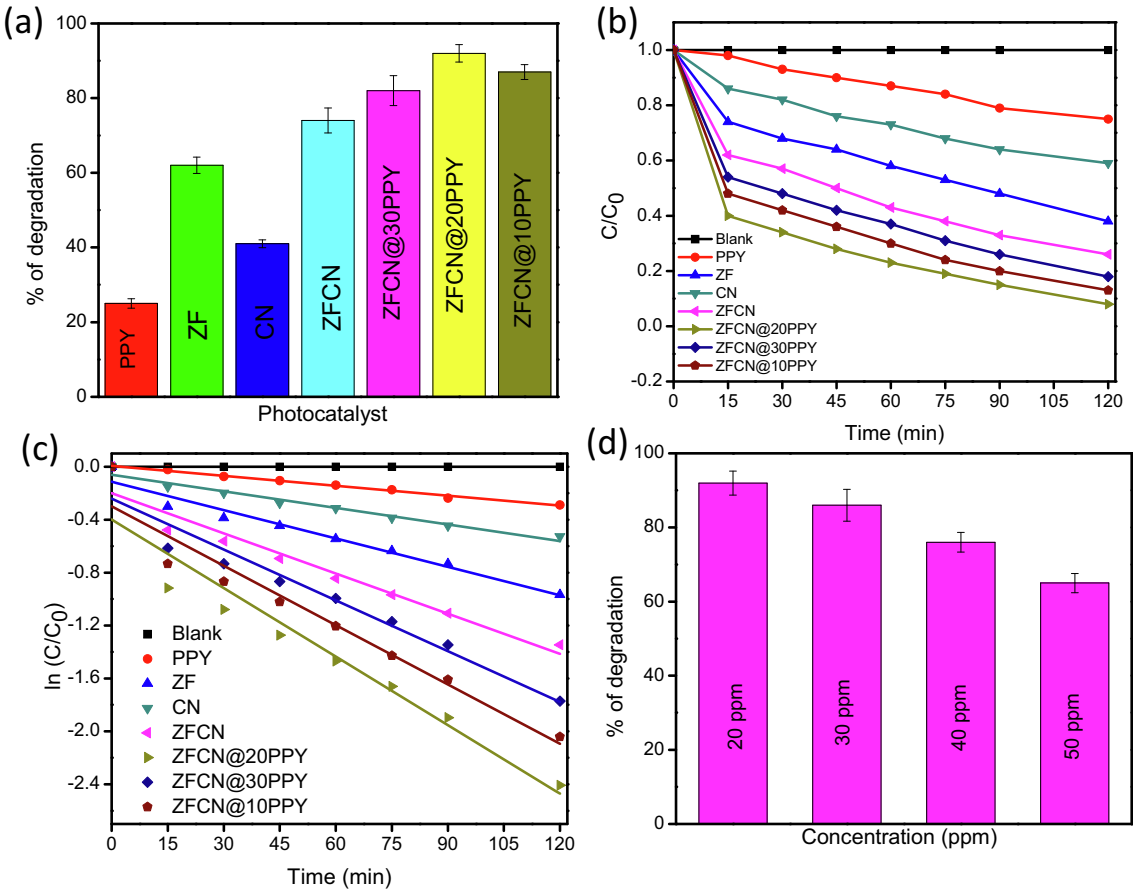

Fig. 9. (a) Ciprofloxacin degradation over synthesized photocatalyst, (b) Ciprofloxacin degradation over synthesized photocatalyst at regular time interval, (c) kinetics of ciprofloxacin degradation, (d) effect of pollutant concentration.

Table 2
K_{app} values and Regression coefficient (R^2) of all the prepared samples for CIP degradation.

Catalysts	k_{aap} (10^{-4} min^{-1}) CIP	Regression co-efficient (R^2)
PPY	23	0.991
ZF	80	0.954
CN	43	0.961
ZFCN	112	0.943
ZFCN@20PPY	215	0.928
ZFCN@30PPY	140	0.934
ZFCN@10PPY	171	0.932

with ciprofloxacin molecules for photons and active sites present on the catalyst surface. The degree of removal efficiency of CIP by the photocatalyst decreases from 92% to 72% upon increasing the pollutant concentration from 20 ppm to 50 ppm. Therefore 20 ppm was found to be an optimum initial concentration of CIP which was used in the experiments.

2.8.2. Photocatalytic H_2 generation

After CIP degradation, the photocatalytic capabilities of the designed samples were further explored towards hydrogen generation under visible light illumination, using an aqueous solution of methanol (hole scavenger). As shown in Fig. 10a, the rate of photocatalytic hydrogen evolution follows the order: PPY (95) < CN (1 1 6) < ZF (2 8 5) < ZFCN (4 1 2) < ZFCN@20PPY (567 μmol/h). It was noticed ZFCN@20PPY shows maximum hydrogen production which can be ascribed to the black color of the sample which absorbs maximum photons as well as effective charge separation via double charge transfer mechanism. Due to the lower energy gap of PPY, it behaves as a photo-sensitizer and supplies a surplus number of electrons to ZFCN heterojunction which leads to a high concentration of photoelectrons and hence improves the rate of hydrogen production. Similarly, a blank experiment was also conducted maintaining the same reaction condition but without any photocatalyst to assure that H_2 evolution occurs in the presence of photocatalyst and light only i.e. the reaction is photocatalytic. Furthermore, the effect of various sacrificial reagents (methanol, ethanol, and ethylene glycol) towards H_2 evolution was studied over the best performing photocatalyst (ZFCN@20PPY). It was observed that 80μmole of hydrogen was evolved without the addition of any sacrificial reagent which was very low in comparison to results obtained in the presence of sacrificial agents. This emphasizes the importance of sacrificial agents (SRs) in hydrogen production. The rate of hydrogen generation over ZFCN@20PPY using different sacrificial reagents follows the order: water (H_2O) < methanol > ethylene glycol > ethanol(Fig. 10b). The results suggest that methanol is the best SRs used in H_2 evolution reaction and the reasons are explained below.

- Carbon number: Maximum H_2 evolution was obtained for methanol whereas lower hydrogen production was obtained for ethylene glycol and ethanol. The output suggests that the carbon content of SRs is inversely proportional to the rate of hydrogen production. With an increase in the carbon chain the rate of H_2 evolution decreases [51].
- Oxidation potential: Along with carbon length, the oxidation potential of the sacrificial agents (SRs) also affects the rate of photocatalytic reaction. Because SRs are known to be the elec-

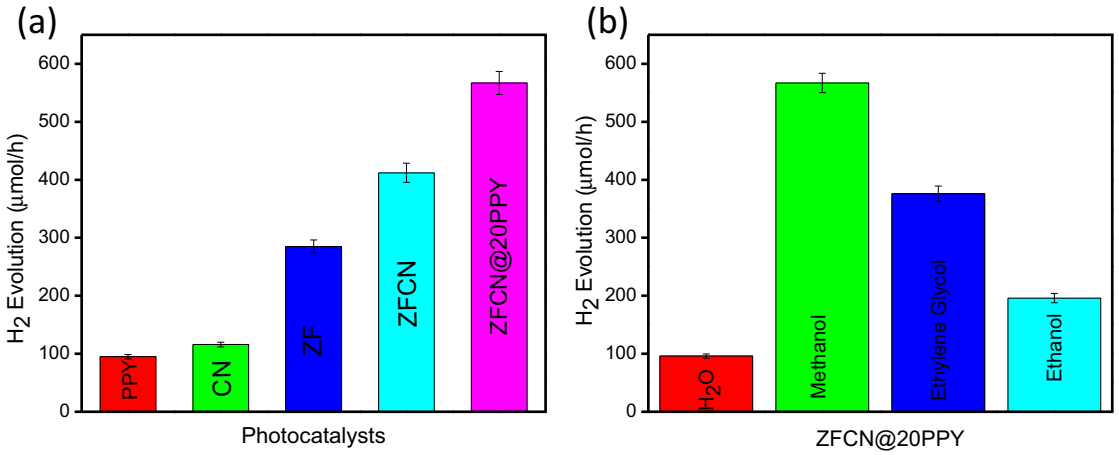

Fig. 10. (a) H_2 evolution rate by various photocatalysts (b) Effect of various sacrificial reagents on hydrogen evolution over ZFCN@20PPY.

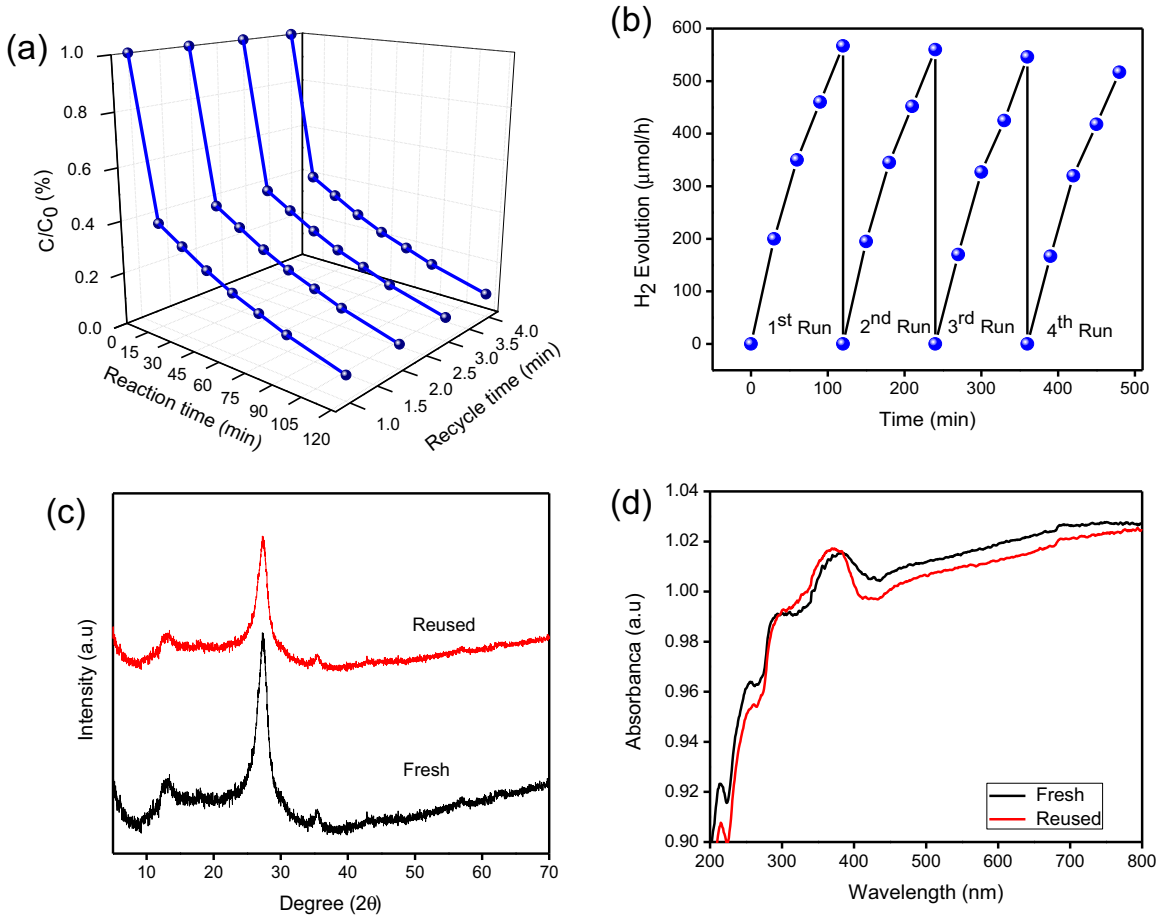

Fig. 11. (a and b) Reusability graph of CIP degradation and H_2 evolution (c) XRD and (d) UV–Vis images of fresh and reused ZFCN@20PPY photocatalyst.

tron donors by consuming the photogenerated holes and hampers the reaction process. This indicates that SRs with low potential can oxidize easily while those with high potential oxidizes poorly. As the oxidation potential of methanol is less, it can easily oxidize and neutralize the photogenerated holes and improves the photocatalytic H_2 evolution [51].

- Permittivity: Similarly, the permittivity of the SRs was also found to affect the H_2 evolution rate. The permittivity of methanol is found to be more than ethanol and maximum H_2 evolution was also encountered in the case of methanol [51].

2.8.3. Reusability and stability experiments

Photo-stability property of photocatalyst is very much important in deciding the efficiency of the material. Hence the reusability test of the prepared photocatalysts was evaluated towards CIP degradation and H_2 evolution. After completion of the performed photocatalytic reaction, the photocatalysts were recovered by centrifugation, washed with deionized water and ethanol and then dried in an oven for further use i.e. for subsequent CIP degradation and H_2 evolution reaction separately. A similar process was repeated up to 4 cycles and results were presented in Fig. 11.

Fig. 11a, b describes that the antibiotic degradation and hydrogen evolution was found to be constant up to the third cycle and then decreases in the fourth cycle. The weight loss of ZFCN@20PPY during the recovery process might be the possible reason behind the decreased photocatalytic activity of reused photocatalyst. Additionally, the binding of the pollutant over the surface of catalyst creates a barrier between the active site and reactive molecule during recycle tests. XRD and UV–Vis characterization of fresh and reused ZFCN@20PPY photocatalyst after the 4th cycle has been provided in Fig. 11c & d. From the comparison characterization images, it was observed that there is no significant changes in the framework of the material which confirms its photo-stability nature. Additionally, the photostability of ZFCN@20PPY was confirmed from the XPS spectra of the used composite, and the result is exhibited in Fig. S8. Obviously, the chemical compositions and valence state (peak position) of ZFCN@20PPY keep unchanged after the photocatalytic reaction. Therefore, the ZFCN@20PPYcomposite has excellent recyclability and photostability for the photodegradation of CIP.

2.9. Proposed mechanism

2.9.1. Determination of active species

Moreover, the reaction intermediates which are responsible for antibiotic degradation were evaluated by the performed trapping experiments. In the typical process, various quenchers such as tertiary butyl alcohol (TBA), citric acid (CA), p-benzoquinone (p-BQ) and dimethyl sulfoxide (DMSO) were employed to trace the reactive species (·OH, h^+, $\cdot O^{2-}$ and e^-) present/formed in the reaction system to carry out the photo-degradation reaction [30]. The detailed data about trapping experiments are presented in Fig. 12. It is well known that the maximum degradation of CIP was achieved in the absence of quenchers. From the plotted results it was informed that the degradation pathway was greatly suppressed by the addition of *p*-benzoquinone. From this, it was confirmed that superoxide ($\cdot O^{2-}$) is mainly responsible for CIP degradation. Further, the addition of TBA leads to trap the hydroxyl radicals from the reaction system and hence reduces the degradation process to some extent which indicates that ·OH radical also has a role to play. However, the quenching of *holes* and *electrons* by the addition of (CA) and (DMSO) doesn't hamper the degradation rate. It was concluded that both superoxide and hydroxyl radical plays a major and minor roles in the degradation process respectively. The confirmatory test of these produced superoxide and hydroxyl were further evaluated by the following tests.

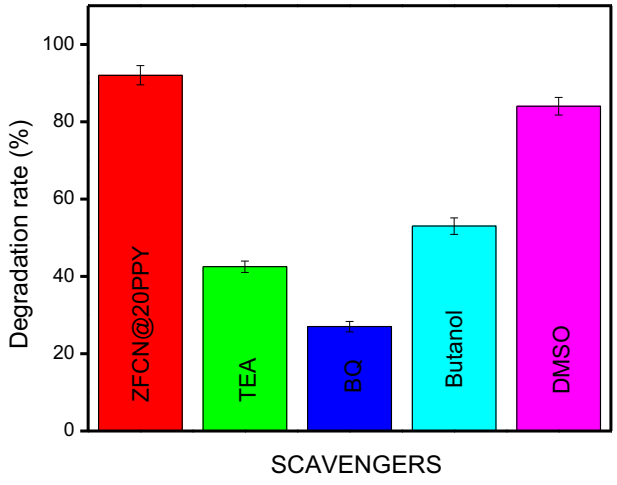

Fig. 12. Degradation study of CIP in presence of different scavengers.

2.9.1.1. NBT experiments. Superoxide confirmatory test was performed by taking NBT as a probe reagent to ascertain the formation and generation of $\cdot O_2^-$ radicals from the surface of the catalyst. Detail procedure of the experiment was followed by our previously reported literature [13]. The suspension of catalyst and NBT was filtered. The absorbance spectra of the filtrate were taken and the results were represented in Fig. 13a. However, it was observed that the intensity of the absorbance spectra is very less compared to spectra of neat NBT which means free NBT gets bonded with formed $\cdot O_2^-$ radicals resulting in a complex formation that shows low optical absorbance. All this above observation proves the generation superoxide over the surface of photocatalysts and hence helps in the degradation process [17].

2.9.1.2. TA experiments. Terephthalic acid (TA) experiments were conducted to figure out the formation of hydroxyl radicals in the reaction mixture. Generally, TA reacts with generated ·OH radicals to form a 2-hydroxyterephthalic acid complex (TAOH) and the formation of this complex can be encountered at λ = 426 nm [28]. In the given Fig. 13b, an intense peak is observed at λ = 429 which confirms the formation and generation of ·OH radicals and supports the degradation process.

2.9.2. Photoluminescence spectra

Photoluminescence spectroscopy could be used as one of the preliminary characterizing tools to elucidate the optical features

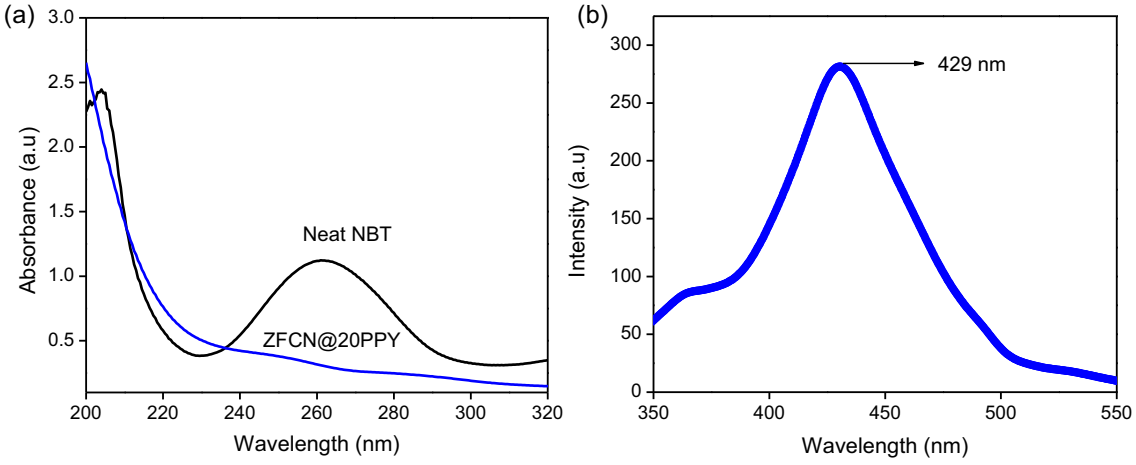

Fig. 13. (a) Absorbance spectra of NBT with and without photocatalyst (b) fluorescence spectrum of ZFCN@20PPY with TA.

of the semiconducting material which gives valuable information about separation, migration and recombination process of the photogeneratedexcitons. In general, the peak intensity is directly proportional to the electron-hole recombination process i.e. intense peak implies faster recombination and *vice versa* [6]. In this study prepared samples are excited at 325 nm and the desired outcomes were portrayed in Fig. 14. A strong and sharp luminescence band encountered at 460 nm for pristine CN which can be ascribed to band-band PL phenomenon originating from n-π^* transition of lone pair electrons over N-atom [18]. This emission was observed for all composite samples with blue shifting and reduced intensity which implies good interaction of CN with its composite counterpart (ZF). Similarly, for neat ZF, an intense peak was visualized at 391 nm corresponding to an ultraviolet band which is attributed to the near-band-edge (NBE) emissions originating from the recombination of excited electron of the localized level below the conduction band with the holes of valence band [52]. The emission peak at 391 nm was observed in all composite materials with reduced intensity. From the plotted PL data, it can be noticed that ZFCN@20PPY exhibits an extremely low intense spectrum as compared to other composites and also parent materials. So, it can be concluded that heterojunction formation between ZF and CN followed by sensitization with PPY helps in slowing down the recombination process and accelerating the migration of excitons within the system. From the above discussion, it was concluded that out of all the synthesized samples ZFCN@20PPY is found to be a better photocatalyst that is well matched with our EIS and photocatalytic performance.

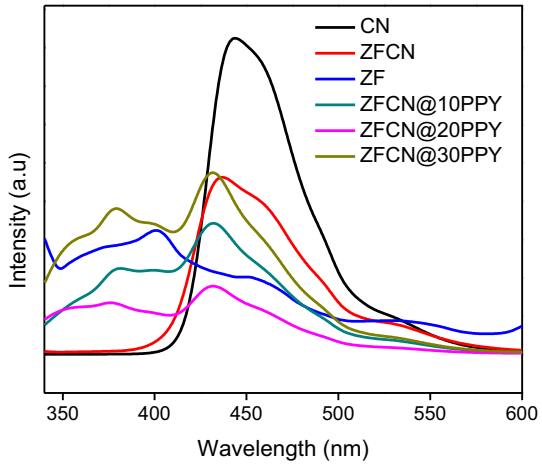

Fig. 14. Luminescence spectra of CN, ZF, ZFCN, ZFCN@10PPY, ZFCN@20PPY and ZFCN@30PPY.

2.9.3. Electrochemical properties

Electrochemical impedance spectroscopy (EIS) is a powerful and non-destructive process used to determine the interfacial charge transfer resistance offered by neat ZF, CN, PPY, ZFCN and ZFCN@20PPY nanocomposites. The Nyquist plot in Fig. 15a shows two sections (i) semicircular geometry found in higher frequency region and (ii) the straight line in the lowfrequency area. The arc radius of ZFCN is small as compared to neat ZF and CN, confirming the successful development of ZFCN n-n heterojunction which can effectively improve the charge separation through an internal electric field and interfacial interaction of ZFCN heterojunction [44]. With respect to ZFCN heterojunction, ZFCN@20PPY shows a small semicircle which indicates low charge transfer resistance or high electrochemical conductivity and the loop in lower frequency indicates the Warburg resistance [28]. The conductivity increases in ZFCN@20PPY nanocomposites which support the easy flow of photo-excited electrons in the electrode-electrolyte interface. From Fig. 15a it was confirmed that in comparison to neat materials the ZFCN@20PPY shows high charge separation efficiency, low resistance, low electron-hole recombination, high conductivity and high photocatalytic activity, which is well supported by PL analysis.

Fig. 15b shows the current-potential curve of neat and ZFCN@20PPY nanocomposites under light illuminations ($\lambda \geq 400$ nm). The neat ZF and CN shows anodic photocurrent density due to applying positive potential which proves the n-type behavior of the electrodes. However, the formation of ZFCN doesn't show any saturation outcome even at a potential higher than 1.23 eV vs. NHE. The absence of saturation effect suggests the development of ZFCN heterojunction which is responsible for efficient charge carrier separation as compared to neat ones [53]. Similarly, the PPY demonstrates the cathodic current density by applying the negative potentials and the final nanocomposites i.e. ZFCN@20PPY shows both anodic and cathodic current density that informs about the presence of n and p-type semiconducting character in the ternary hybrid. Further, the n- and p-type behavior is confirmed by M-S analysis. The fabricated photocatalysts (CN, ZF and ZFCN) shows n-type photocurrent density i.e. 1.4, 1.5 and 1.9 mA/cm^2 whereas PPY produces a cathodic current density (p-type nature) of −1.6 mA/cm^2 respectively. Interestingly, ZFCN@20PPY hybrid displays a cathodic current density of −3.93

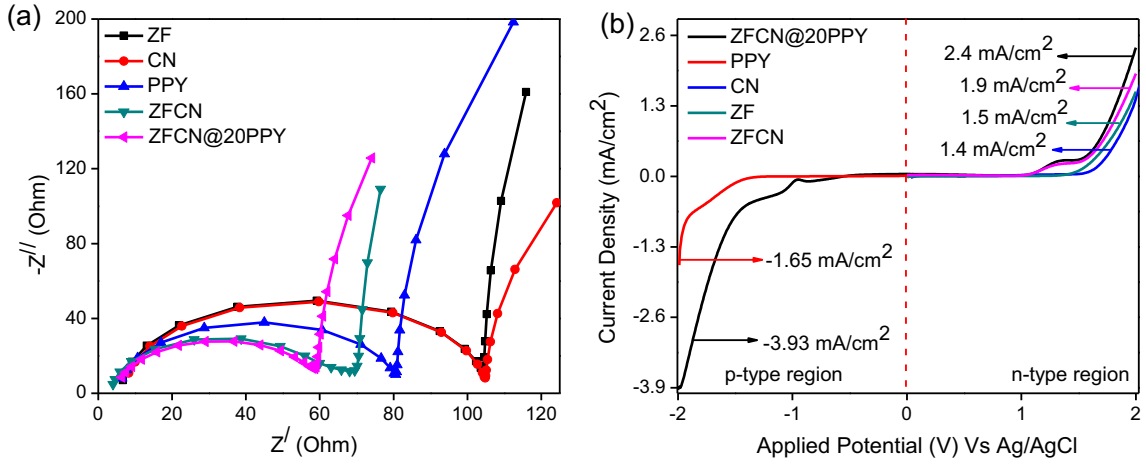

Fig. 15. (a) EIS and (b) LSV plots of PPY, CN, ZF, ZFCN and ZFCN@20PPY.

and an anodic current value of 2.4 mA/cm^2 respectively. The highest photocurrent density of the ZFCN@20PPY nanocomposites showed maximum charge separation and high photocatalytic activity which may be due to the addition of PPY. This photochemical behavior is well supported by PL and EIS analysis.

To figure out the flat band potential along with the type of semiconducting material, Mott- Schottky measurements were carried out and the obtained results were depicted in Fig. 16. As we know that different semiconducting materials have different Fermi levels. The formation of composite leads to the formation of a new energy level due to the movement of Fermi levels of the co-joined semiconductors. The new Fermi level formed favors the interfacial exchange of charge carriers and also results in an interfacial electric field [54]. Positive slopes obtained by drawing a tangent to potential X-axis indicate the n-type behavior of ZF and CN (Fig. 16a and b) while negative slope was obtained for PPY (Fig. S9). Similarly, a positive slope was obtained after extra-polatting the tangent to X-axis and the value of flat band potential of $ZnFe_2O_4$/g-C_3N_4 is found to be in between the flat band potential of $ZnFe_2O_4$ and g-C_3N_4 as shown in supporting information (Fig. S10). The obtained positive M-S plot for $ZnFe_2O_4$/g-C_3N_4 (ZFCN) confirms about the formation of n-n heterojunction. The flat band potential for ZFCN is found to be −0.75 eV Ag/AgCl respectively. Additionally, the LSV study of $ZnFe_2O_4$/g-C_3N_4 also shows only n-type of current which suggests the prepared composite is n-n based photocatalyst. The band potentials of ZF, CN and PPY are found to be −0.61, −1.55 and −0.35 eV Vs Ag/AgCl respectively. The obtained band potential can be converted into NHE (normal hydrogen electrode) using the equation mentioned in electrochemical characterization techniques. Thus, the CB potentials of ZF, CN and PPY were computed to be −0.06, −1.0 and −1.22 eV while the corresponding VB potentials were calculated to be 1.74, 1.68, 0.20 eV respectively Vs NHE. Based on the theoretical energy diagram, appropriate charge separation and possible photocatalytic mechanism of polymer sensitized n-n heterojunction have been schematically demonstrated in Fig. 16c.

2.9.4. Proposed mechanism of ZFCN@20PPY photocatalyst

As anticipated, PPY decorated on ZFCN n-n heterojunction shows enhanced photocatalytic activity in comparison to other samples which can be attributed to factors like the ability to absorb a broad range of the solar spectrum, effective generation of active species and productive charge separation. In ZFCN heterojunction both CN and ZF can be excited under visible light illumination to produce electron and holes. In detail, CN on excitation stimulates π-π* transition to produce photo-excited electrons from VB to CB, while in case of ZF, the electrons get excited from the VB (2p orbital of O-atom) to the empty 3d orbital of Fe (CB), leaving the holes behind [54,55]. From M-S studies and theoretical energy diagram as shown in Fig. 16, it was found that the CB potentials of CN are more negative than the CB potential of ZF. Combining with the band gap energies as revealed in Fig. S1, the VB potentials of CN and ZF are estimated and indicate that the ZFCN composite belongs to a type-II heterostructure group. The working principle of the

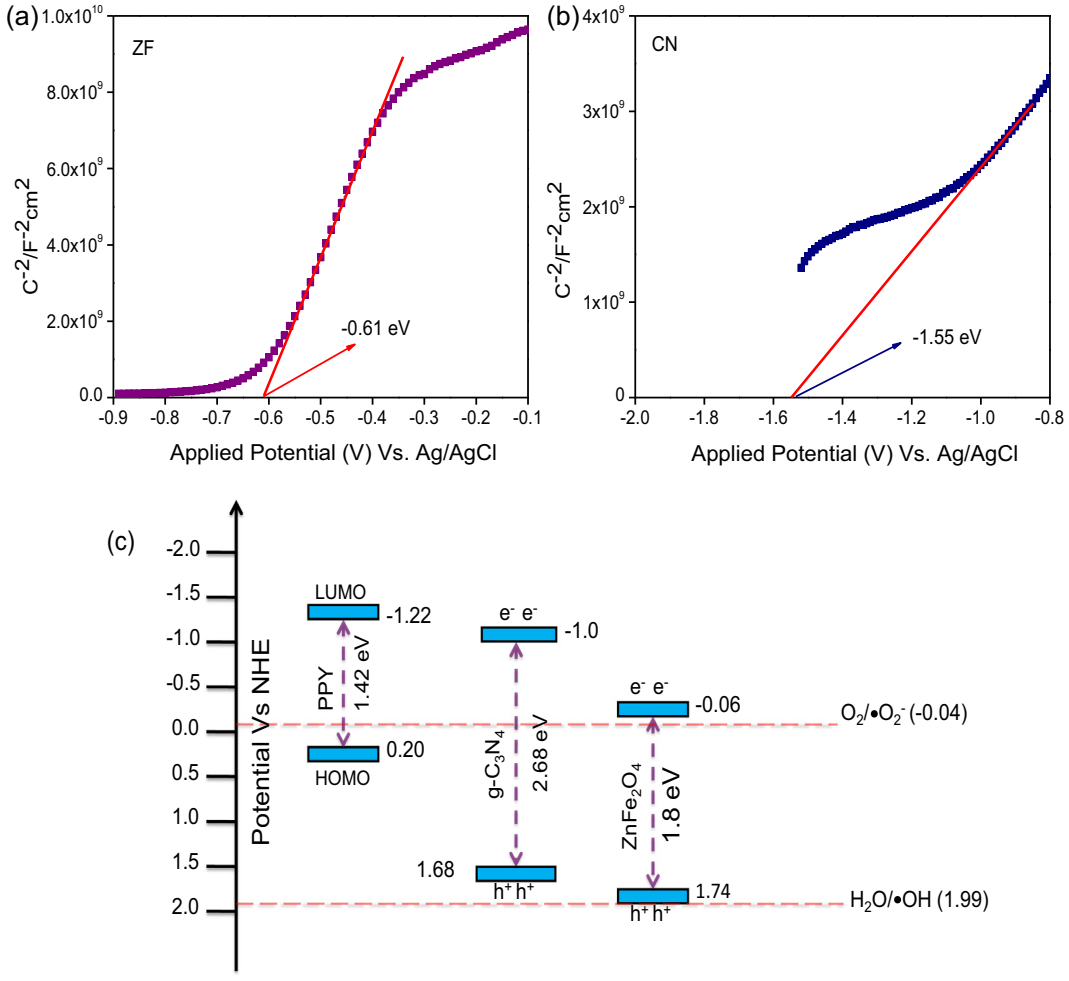

Fig. 16. Mott-Schottky graph of (a) ZF (b) CN and (c) band edge potentials of PPY, CN and ZF.

photocatalyst can be well explained by a double charge transfer mechanism, potential level, and sensitizer phenomenon. The CB position of CN is situated at more negative value as compared to the CB position of ZF, so photo-excited electron will shift from CB of CN to ZF by an offset of 0.94 eV while the left-over holes will move from VB of ZF to CN driven by offset of 0.06 eV. Thus, the potential difference in the n-n heterojunction material plays a significant task in the charge separation &channelization process. It has been reported that redox potential of $O2/\cdot O_2^-$ is −0.046 eV Vs NHE which is more positive than the E_{CB} of CN and ZF. As a result, the photogenerated electrons present on the surface of photocatalyst can easily convert the dissolved oxygen to highly reactive super oxide ($\cdot O_2^-$) radicals. The holes remaining in the VB of ZF get transferred to the VB of CN to reduce the accumulation of photogenerated holes on the ZF surface. As the VB potential of CN (1.64 eV) is not favorable for direct ·OH ($OH^-/\cdot OH$ = 1.99 eV) formation, but trapping experiment confirms that super oxide and hydroxyls are the main causal agents responsible for CIP degradation. So, it can be said that that hydroxyl radicals may be produced indirectly by the reaction of superoxide with H^+. Now moving on to the sensitizer effect, when photocatalyst (ZFCN@20PPY)was irradiated under solar spectrum both ZF and CN get excited to generate excitons. In the meantime, polypyrrole (sensitizer) present in the ZFCN heterojunction (ZFCN@20PPY) also absorbs light energy to initiate the production of the electron from the highest occupied molecular orbit (HOMO(π)) and transfer to the lowest unoccupied molecular orbital (LUMO(π*)). The π orbital of polypyrrole acts as a valence band (HOMO) while the π* orbital acts as a conduction band (LUMO). Thus upon excitation, the charge carriers get excited from HOMO and jumps to LUMO owing to π-π* transition [56,57]. From the UV spectrum and Tauc plot, the energy gap of the polymer was determined to be 1.43 eV. With the help of M-S measurement, the energy plane of HOMO and LUMO of PPY was calculated to be 0.20 and −1.22 eV. From the output results, it has been clarified that HOMO and LUMO potentials of PPY are found to be situated at a higher position than the VB and CB offsets of CN and ZF respectively. Upon excitation, the electrons get excited and it readily migrates to the CB of CN as well as ZF. Similarly, photon induced charge carriers from the conduction potential of CN are injected into the CB potential of ZF. As a result huge amount of electrons from PPY and CN along with self-excited electrons gets accumulated at the Fe 3d orbital (CB) of ZF from where the photogenerated electrons were further captured by the molecular oxygen present in the reaction system to generate reactive oxygen species like superoxide and hydroxyl, that are responsible for pollutant degradation as demonstrated in Scheme 1. The left-over hole in the PPY also oxidizes the antibiotic to some extent. In this manner, the electrons and holes are properly used to degrade pollutants and reduce the recombining possibility of the photogenerated electron with holes. In H_2 evolution only electrons take part in the photolysis of water. The holes produced are being removed from the reaction medium by the help of quencher (methanol, ethanol and ethylene glycol). As a result, only electrons are available in the reaction systems which are readily captured by H^+ to produce H_2. ZFCN@20PPY exhibits the highest amount of H_2 gas in comparison to others which can be ascribed to the presence of PPY. Both CIP degradation and H_2 generation are found to be highest for ZFCN@20PPY which is well matched with our PL, EIS and LSV data.

$$\text{ZFCN@PPY} + h\upsilon \rightarrow (e^-) + (h^+)$$

$$\text{ZFCN@PPY}\ (e^-) + O_2 \rightarrow \cdot O_2^-$$

$$H_2O \leftrightarrow H^+ + OH^-$$

$$\text{ZF/CN/PPY}\ (e^-) + \cdot O_2^- + 2H^+ \rightarrow H_2O_2$$

$$\text{ZF/CN/PPY}\ (e^-) + H_2O_2 \rightarrow \cdot OH + OH^-$$

$$\text{CIP} + \cdot OH \rightarrow \text{degraded products}$$

$$\text{CIP} + \cdot O_2^- \rightarrow \text{degraded products}$$

The net reaction is

$$\text{Ciprofloxacin} + \cdot OH + (\cdot O_2^-) \rightarrow \text{degraded products}$$

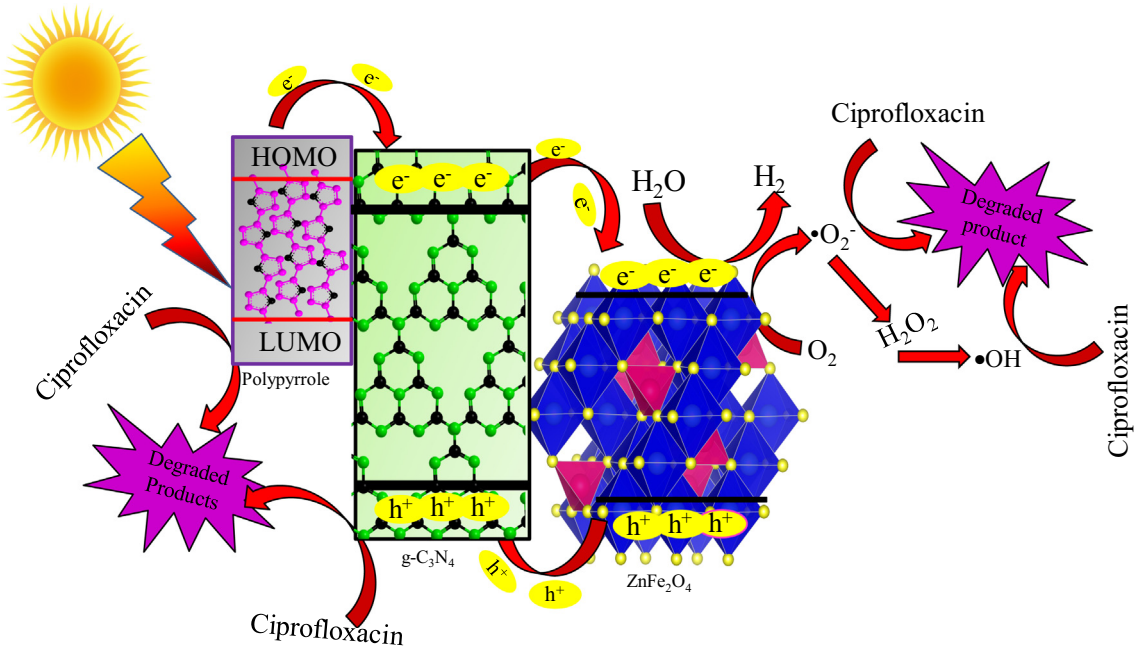

Scheme 1. Schematic representation of CIP degradation and H_2 evolution.

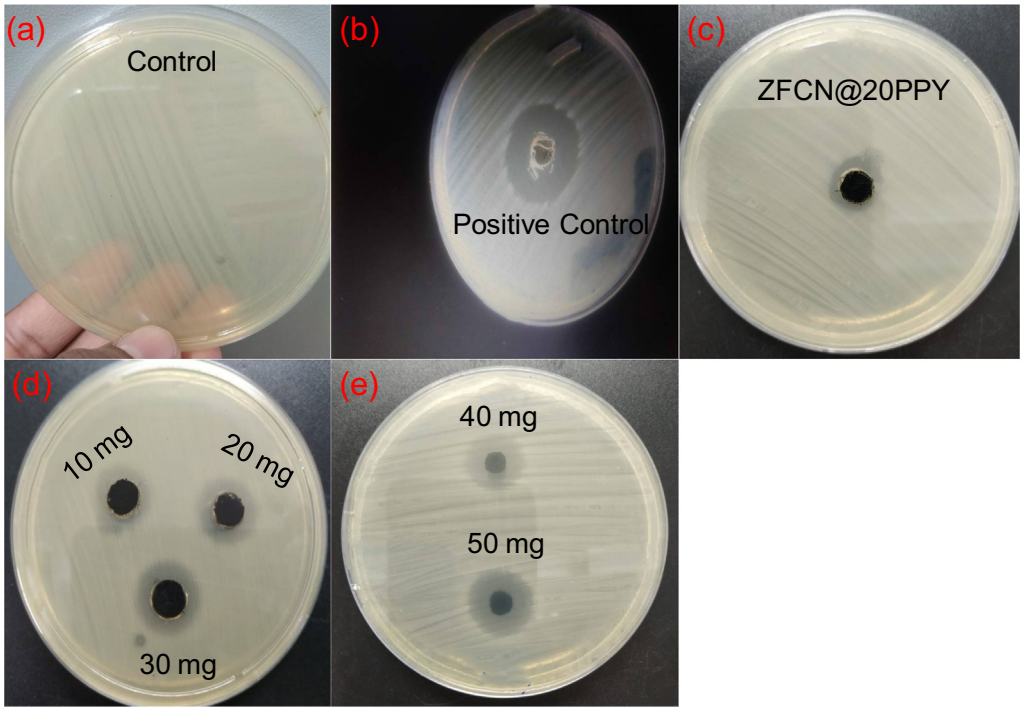

Fig. 17. (a) Growth of bacterial colonies, antibacterial activity evaluated in terms of (ZOI) of (b) standard antibiotic (amoxicillin) (c-e) ZFCN@20PPY and it's different concentration.

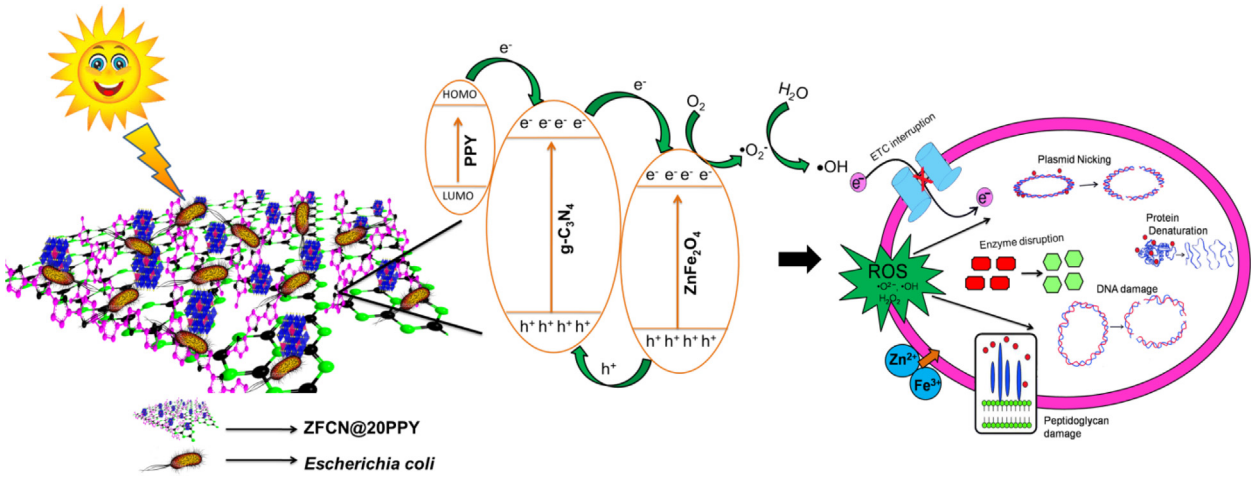

Scheme 2. Schematic representation of role of reactive oxygen species in damaging some vital micro-molecules of bacterial cell.

2.10. Antibacterial studies

To explore the antibacterial properties of the ZFCN@20PPY, the composite was tested against a common pathogenic bacterium namely *Escherichia coli* by well diffusion method and the outcomes were shown in Table 3 and Fig. 17. However, the antibacterial activity of ZFCN@20PPY was compared with a regular antibiotic like Amoxicillin (0.5 mg) which has been considered as a positive control. However, after the incubation period, the complete growth of *E. coli* can be seen from Fig. 17a, in absence of nanocomposite and antibiotic. But after the introduction of Amoxicillin and ZFCN@20PPY (Fig. 17b and c), a clear & distinct circular zone was observed for both cases which specify that along with an antibiotic, the synthesized material inhibits the growth of *E. coli*. The outcomes displayed in Fig. 17(d and e) reveals the inhibition size or the clearance zone increases upon increasing the amount of nanocomposite. The principal mechanism behind antibacterial activity can be ascribed to the formation of reactive oxygen species

Table 3
Zone of inhibition of antibacterial activity by different concentration of synthesized ZFCN@20PPY compared with standard antibiotic.

Name of the Strain	Sample	Concentration (mg/mL)	Zone of Inhibition (mm)
Escherichia coli (ATCC 8739)	ZFCN@20PPY	10	7
		20	8
		30	10
		40	12
		50	17
	Amoxicillin	0.5	27

(ROS) like super oxide, hydroxyl, hydrogen peroxide and singlet oxygen upon irradiation with visible light as shown in scheme 2 [48]. These ROS induces the oxidative stress which is responsible for inhibiting the growth of bacterial colonies by damaging their biological components like enzyme, proteins, and DNA [58,59]. Similar results were reported by Kim et al, where indirectly formed hydroxyl radicals damage the biological micro-molecules [60]. Moreover, previous literature suggests nanoparticles ranging in the range of 10–80 nm can enters into the bacteria cell through a bacterial membrane and leads to the destruction of bacterial cell [61]. Additionally, the metal ions Zn^{2+} and Fe^{3+} present in the sample is easily attracted by the negatively charged cell membrane of bacteria which leads to the death of bacterial cell by damaging it's DNA replication process and protein denaturation [62]. However, the synthesized sample shows good antibacterial properties as compared to antibiotic and hence can be utilized in the medical sector against the bacteria.

3. Conclusion

In brief, we have synthesized an n-n zinc ferrite/graphitic carbon nitride (ZFCN) heterojunction photocatalyst, by in-situ calcinations method and further modified with polypyrrole (PPY) by oxidative polymerization technique. The developed photo catalysts were tested towards ciprofloxacin degradation, hydrogen evolution and antibacterial studies under visible light illumination. Further, the amount of polymer content in ZFCN significantly influence the photon absorption, charge separation and photocatalytic behavior of the material as justified via UV–Vis DRS, PL, EIS and photocatalytic study. Additionally, 20 wt% polymer loaded zinc ferrite/graphitic carbon nitride shows maximum activity i.e. 92% ciprofloxacin degradation, 567 μmol/h hydrogen energy evolution and notable antibacterial activity against *Escherichia coli* (ATCC-8739) compared to reported values [63]. The principal cause behind such high photocatalytic performance is attributed to polypyrrole loading and double charge transfer mechanism leading to wide light absorption range and effective excitons separation respectively. It is believed that the present investigations will give a new hope to scientific community by utilizing polymer based materials to solve energy crisis and environmental problems.

Declaration of Competing Interest

There is no conflict to declare.

Acknowledgements

The authors are very much thankful to the management of S'O'A (Deemed to be University) for their encouragement and support.

Appendix A. Supplementary material

The supporting information is also available from the author containing materials and synthesis procedure, formation mechanism, characterization techniques, photocatalytic experiments, scavenger experiment, antibacterial studies procedure, Fig. S1 Plots of $(\alpha h\nu)2$ vs. photon energy ($h\nu$) for the band gap energy of (a) CN (b) ZF (c) PPY (d) ZFCN (e) ZFCN@20PPY, Fig. S2 TEM and SAED images of ZF, CN and PPY (a–g), Fig. S3 SEM images of ZF, CN and PPY (a–d), Fig. S4 XPS survey scan of ZFCN@20PPY, Fig. S5 EDX spectra of ZFCN@20PPY, Fig. S6 Raman spectra of (a) PPY and (b) CN, Fig. S7 (a) Absorbance spectra of CIP over ZFCN@20PPY (b) HPLC image and (c) TOC image, Fig. S8 XPS spectra of ZFCN@20PPY before and after degradation process, Fig. S9 M-S plot of PPY, Fig. S10 M-S plot of ZFCN. Supplementary data to this article can be found online at https://doi.org/10.1016/j.jcis.2019.11.030.

References

[1] Y.A. Sethi, R.P. Panmand, A.A. Ambalkar, A.K. Kulkarni, A. Gunjal, D.R. Patil, S.W. Gosavi, M.V. Kulkarni, B.B. Kale, Sustainable Energy Fuels 3 (2019) 793–800.
[2] P.S. Kumar, J. Sundaramurthy, S. Subramanian, V.J. Babu, G. Singh, S.I. Allakhverdiev, S. Ramakrishna, Energy Environ. Sci. 7 (2014) 3192–3222.
[3] C. Li, Y. Xu, W. Tu, G. Chen, R. Xu, Green Chem. 19 (2017) 882.
[4] X. Liu, J. Iocozzia, Y. Wang, X. Cui, Y. Chen, S. Zhao, Z. Li, Z. Lin, Energy Environ. Sci. 10 (2017) 402–434.
[5] S. Yang, D. Xu, B. Chen, B. Luo, W. Shi, Appl. Catal., B: Environ. 204 (2017) 602–610.
[6] S. Mansingh, R. Acharya, S. Martha, K.M. Parida, Phys. Chem. Chem. Phys. 20 (2018) 9872–9885.
[7] C. Li, Z. Sun, W. Zhang, C. Yu, S. Zheng, Appl. Catal., B: Environ. 220 (2018) 272–282.
[8] D.P. Sahoo, S. Nayak, K.H. Reddy, S. Martha, K.M. Parida, Inorg. Chem. 57 (2018) 3840–3854.
[9] D.P. Sahoo, S. Patnaik, D. Rath, K.M. Parida, Inorg. Chem. Front. 5 (2018) 879–896.
[10] P. Mishra, A. Behera, D. Kandi, K.M. Parida, Nanoscale Adv. 1 (2019) 1864–1879.
[11] C. Liang, C.G. Niu, M.C. Shen, S.F. Yang, G.M. Zeng, New J. Chem. 42 (2018) 3270–3281.
[12] S. Mansingh, D.K. Padhi, K.M. Parida, Int. J. Hydrogen Energy 41 (2016) 14133–14146.
[13] H. Yi, M. Yan, D. Huang, G. Zeng, C. Lai, M. Li, X. Huo, L. Qin, S. Liu, X. Liu, B. Li, H. Wang, M. Shen, Y. Fu, X. Guo, Appl. Catal., B: Environ. 250, 52–62.
[14] H. Yi, D. Huang, G. Zeng, C. Lai, L. Qin, M. Cheng, S. Ye, B. Song, X. Ren, X. Guo, Appl. Catal., B: Environ. 239 (2018) 408–424.
[15] H. Yi, M. Jiang, D. Huang, G. Zeng, C. Lai, L. Qin, C. Zhou, B. Li, X. Liu, M. Cheng, W. Xue, P. Xu, C. Zhang, J. Taiwan Inst. Chem. Engrs. 93 (2018) 184–192.
[16] H. Wang, Z. Zeng, P. Xu, L. Li, G. Zeng, R. Xiao, Z. Tang, D. Huang, L. Tang, C. Lai, D. Jiang, Y. Liu, H. Yi, L. Qin, S. Ye, X. Ren, W. Tang, Chem. Soc. Rev. 48 (2019) 488.
[17] A. Behera, S. Mansingh, K.K. Das, K.M. Parida, J. Colloid Interface Sci. 544 (2019) 96–111.
[18] S. Patnaik, K.K. Das, A. Mohanty, K. Parida, Catal. Today 315 (2018) 52–66.
[19] H. Song, L. Zhu, Y. Li, Z. Lou, M. Xiao, Z. Ye, J. Mater. Chem. A 3 (2015) 8353–8360.
[20] D.P. Sahoo, S. Patnaik, D. Rath, B. Nanda, K.M. Parida, RSC Adv. 6 (2016) 112602–112613.
[21] Y. Li, Y. Xue, J. Tian, X. Song, X. Zhang, X. Wang, H. Cui, Sol. Energy Mater. Sol. Cells 168 (2017) 100–111.
[22] Y. Yang, C. Zhang, D. Huang, G. Zeng, J. Huang, C. Lai, C. Zhou, W. Wang, H. Guo, W. Xue, R. Deng, M. Cheng, W. Xiong, 245 (2019) 87–99.
[23] M.Q. Wen, T. Xiong, Z.G. Zang, W. Wei, X.T. Tang, F. Dong, Opt. Exp. 24 (2016) 10205–10212.
[24] Q. Chen, Q. He, M. Lv, X. Liu, J. Wang, J. Lv, Appl. Surf. Sci. 311 (2014) 230–238.
[25] P. Xiong, L. Wang, X. Sun, B. Xu, Xin Wang, Ind. Eng. Chem. Res. 52 (2013) 10105–10113.
[26] F. Deng, X. Lu, X. Pei, X. Luo, S. Luo, D.D. Dionysiou, J. Hazard. Mater. 332 (2017) 149–161.
[27] Y. Liang, X. Wang, W. An, Y. Li, J. Hu, W. Cui, Appl. Surf. Sci. 466 (2019) 666–672.
[28] K.K. Das, S. Patnaik, B. Nanda, A.C. Pradhan, K.M. Parida, ChemistrySelect 4 (2019) 1806–1819.
[29] W. Zhao, Y. Wang, A. Wang, J. Qian, W. Zhu, S. Dou, A. Chen, RSC Adv. 7 (2017) 7658–7670.
[30] I.C. Ciobotaru, E. Matei, C.C. Ciobotaru, S. Polosan, Synth. Met. 198 (2014) 323–328.
[31] S. Patnaik, D.P. Sahoo, L. Mohapatra, S. Martha, K.M. Parida, Energy Technol. 5 (2017) 1687–1701.
[32] G. Tong, F. Du, W. Wu, R. Wu, F. Liu, Y. Liang, J. Mater. Chem. B 1 (2013) 2647–2657.
[33] C. Esmaeili, M. Ghasemi, L.Y. Heng, S.H. Hassan, M.M. Abdi, W.R.W. Daud, A.F. Ismail, CarbohydrPolym. 114 (2014) 253–259.
[34] S. Zhang, J. Li, M. Zeng, G. Zhao, J. Xu, W. Hu, X. Wang, ACS Appl. Mater. Interfaces 5 (2013) 12735–12743.
[35] A.A.P. Khan, A. Khan, M.M. Rahman, A.M. Asiri, M. Oves, Int. J. Biol. Macromol. 98 (2017) 256–267.
[36] B. Vellaichamy, P. Periakaruppan, R. Arumugam, K. Sellamuthu, B. Nagulan, J. Colloid Interface Sci. 514 (2018) 376–385.
[37] J. Ding, W. Xu, H. Wan, D. Yuan, C. Chen, L. Wang, W.L. Dai, Appl. Catal. B: Environ. 221 (2018) 626–634.
[38] G. Tzvetkov, M. Tsvetkov, T. Spassov, Superlattices Microstruct. 119 (2018) 122–133.
[39] A. Pruna, Q. Shao, M. Kamruzzaman, Y.Y. Li, J.A. Zapien, D. Pullini, A. Ruotolo, Appl. Surf. Sci. 392 (2017) 801–809.
[40] L. Li, H. Bi, S. Gai, F. He, P. Gao, Y. Dai, X. Zhang, D. Yang, M. Zhang, P. Yang, Sci. Rep. 7 (2017) 43116.
[41] H. Lv, L. Ma, P. Zeng, D. Ke, T. Peng, J. Mater. Chem. 20 (2010) 3665–3672.
[42] L. Sun, R. Shao, L. Tang, Z. Chen, J. Alloys Compd. 564 (2013) 55–62.

[43] X. Zhou, X. Li, H. Sun, P. Sun, X. Liang, F. Liu, G. Lu, ACS Appl. Mater. Interfaces 7 (2015) 15414–15421.
[44] N. Tian, H. Huang, C. Liu, F. Dong, T. Zhang, X. Du, S. Yua, Y. Zhang, J. Mater. Chem. A 3 (2015) 17120.
[45] M. Setka1, R. Calavia, L. Vojkůvka, E. Llobet, J. Drbohlavová, S. Vallejos, Sci. Rep. 9 (2019) 8465.
[46] A. Hayat, F. Raziq, M. Khan, I. Ullah, M.U. Rahmana, W.U. Khan, J. Khan, A. Ahmad, J. Photochem. Photobiol A. 379 (2019) 88–98.
[47] J.M. Lee, J.H. Yang, N.H. Kwon, Y.K. Jo, J.H. Choy, S.J. Hwang, Dalton Trans. 47 (2018) 2949–2955.
[48] C. Han, R. Shi, D. Zhou, H. Li, L. Xu, T. Zhang, B. Li, ACS Appl. Mater. Interfaces 11 (2019) 15646–15655.
[49] W. Wua, J. Dan Wei, D. Zhua, F. Niu, L. Wang, L. Wang, P. Yang, C. Wang Yang, Ceram. Int. 45 (2019) 7328–7337.
[50] F. Dong, Z. Zhao, T. Xiong, Z. Ni, W. Zhang, Y. Sun, W.K. Ho, ACS Appl. Mater. Interfaces 5 (2013) 11392–11401.
[51] M. Wang, S. Shen, L. Li, Z. Tang, Junhe Yang, J. Mater. Sci. 52 (2017) 5155–5164.
[52] M. Ashokkumar, S. Muthukumaran, J. Magn. Magn. Mater 374 (2015) 61–66.
[53] C. Sada, S. Turner, Y. Gönüllü, T.P. Ruoko, L. Borgese, E. Bontempi, S. Mathur, Adv. Mater. Interfaces 2 (2015) 1500313.
[54] X. Yang, F. Qian, G. Zou, M. Li, J. Lu, Y. Li, M. Bao, Appl. Catal. B: Environ. 193 (2016) 22–35.
[55] T. Yang, J. Xue, H. Tan, A. Xie, S. Li, W. Yan, Y. Shen, Highly ordered ZnO/$ZnFe_2O_4$ inverse opals with binder-free heterojunction interfaces for high-performance photoelectrochemical water splitting, J. Mater. Chem. A 6 (2018) 1210–1218.
[56] Y. Liu, H. Zhang, Y. Lu, J. Wu, B. Xin, Catal. Commun. 87 (2016) 41–44.
[57] H. Han, M. Fu, Y. Li, W. Guan, P. Lu, X. Hu, Chinese J. Catal. 39 (2018) 831–840.
[58] D.K. Padhi, T.K. Panigrahi, K.M. Parida, S.K. Singh, P.M. Mishra, ACS Sustainable Chem. Eng. 5 (2017) 10551–10562.
[59] M. Chauhan, B. Sharma, R. Kumar, G.R. Chaudhary, A.A. Hassan, S. Kumar, Environ Res 168 (2019) 85–95.
[60] C. Lee, J.Y. Kim, W. Lee, K.L. Nelson, J. Yoon, D.L. Sedlak, Environ. Sci. Technol. 42 (2008) 4927–4933.
[61] Danie'leTouati, Arch. Biochem. Biophys. 373 (2000) 1–6.
[62] M.M. Naik, H.S.B. Naik, G. Nagaraju, M. Vinuth, H.R. Naika, K. Vinu, Microchem. J. 146 (2019) 1227–1235.
[63] A. Behera, D. Kandi, S. Mansingh, S. Martha, K. Parida, J. Colloid Interface Sci. 556 (2019) 667–679.